



Article

A Distributed Sensing- and Supervised Deep Learning-Based Novel Approach for Long-Term Structural Health Assessment of Reinforced Concrete Beams

Minol Jayawickrema ^{1,2,3}, Madhubhashitha Herath ^{1,4}, Nandita Hettiarachchi ⁵, Harsha Sooriyaarachchi ⁶, Sourish Banerjee ², Jayantha Epaarachchi ^{1,2,*} and B. Gangadhara Prusty ^{7,8}

- Centre for Future Materials, University of Southern Queensland, Toowoomba, QLD 4350, Australia; minol@uwu.ac.lk (M.J.); m.herath@hull.ac.uk (M.H.)
- School of Mechanical and Electrical Engineering, Faculty of Health, Engineering and Sciences, University of Southern Queensland, Toowoomba, QLD 4350, Australia; sourish.banerjee@unisq.edu.au
- Department of Engineering Technology, Faculty of Technological Studies, Uva Wellassa University, Badulla 90000, Sri Lanka
- School of Engineering, Faculty of Science and Engineering, University of Hull, Hull HU6 7RX, UK
- Department of Mechanical and Manufacturing Engineering, Faculty of Engineering, University of Ruhuna, Galle 80000, Sri Lanka; nandita@mme.ruh.ac.lk
- Department of Civil and Environmental Engineering, Faculty of Engineering, University of Ruhuna, Galle 80000, Sri Lanka; harsha@cee.ruh.ac.lk
- School of Mechanical and Manufacturing Engineering, University of New South Wales, Sydney, NSW 2052, Australia; g.prusty@unsw.edu.au
- ARC Training Centre for Automated Manufacture of Advanced Composite, School of Mechanical and Manufacturing Engineering, University of New South Wales, Sydney, NSW 2052, Australia
- * Correspondence: jayantha.epaarachchi@unisq.edu.au; Tel.: +61-746311372

Abstract

Access to significant amounts of data is typically required to develop structural health monitoring (SHM) systems. In this study, a novel SHM approach was evaluated, with all training data collected solely from a validated finite element analysis (FEA) of a reinforced concrete (RC) beam and the structural health based on the tension side of a rebar under flexural loading. The developed SHM system was verified by four-point bending experiments on three RC beams cast in the dimensions of 4000 mm \times 200 mm \times 400 mm. Distributed optical fibre sensors (DOFS) were mounted on the concrete surface and on the bottom rebar to maximise sample points and investigate the reliability of the strain data. The FEA model was validated using a single beam and subsequently used to generate labelled SHM strain data by altering the dilation angle and rebar sizes. The generated strain data were then used to train an artificial neural network (ANN) classifier using deep learning (DL). Training and validation accuracy greater than 98.75% were recorded, and the model was trained to predict the tension state up to 90% of the steel yield limit. The developed model predicts the health condition with the input of strain data acquired from the concrete surface of reinforced concrete beams under various loading regimes. The model predictions were accurate for the experimental DOFS data acquired from the tested beams.

Keywords: reinforced concrete; distributed fibre optic sensing; deep learning; artificial neural networks; structural health monitoring

check for updates

Academic Editors: Steve Vanlanduit and Yuanchen Zeng

Received: 15 May 2025 Revised: 29 June 2025 Accepted: 30 June 2025 Published: 3 July 2025

Citation: Jayawickrema, M.; Herath, M.; Hettiarachchi, N.; Sooriyaarachchi, H.; Banerjee, S.; Epaarachchi, J.; Prusty, B.G. A Distributed Sensingand Supervised Deep Learning-Based Novel Approach for Long-Term Structural Health Assessment of Reinforced Concrete Beams. *Metrology* 2025, 5, 40. https://doi.org/10.3390/metrology5030040

Copyright: © 2025 by the authors. Licensee MDPI, Basel, Switzerland. This article is an open access article distributed under the terms and conditions of the Creative Commons Attribution (CC BY) license (https://creativecommons.org/licenses/by/4.0/).

1. Introduction

SHM reduces maintenance costs and helps prevent irreparable damage. Therefore, SHM is essential and relevant today, as it prevents considerable deterioration by finding

Metrology **2025**, 5, 40 2 of 29

irregularities as soon as possible. The early detection of structural faults extends service life and reduces repair expenses. An SHM approach entails gathering structural response data over time and analysing these data to identify characteristics that may convey information about the occurrence and extent of potential damage. Large infrastructures such as bridges [1–3], pipelines [4–6], tunnels [7–9], and buildings [10,11] need SHM and associated systems to avoid catastrophic failures during their operational lifetime. Beyond these conventional applications, SHM has demonstrated significant utility in specialised fields like hydraulic engineering, contributing substantially to the structural safety assessment of critical infrastructure such as water dams and hydraulic power plants. For instance, distributed optical fibre sensors are effectively utilised for modal analysis based on dynamic strain measurements in such large-scale structures [12], while spatiotemporal analysis aids in predicting deformation behaviour in complex structures like super-high arch dams [13]. The principles and methodologies leveraged in this study, particularly the use of distributed sensing and data-driven assessment, align well with the advanced SHM needs observed across various engineering disciplines, including hydraulic structures.

The scope of SHM further extends to diverse methodologies and sensing technologies for damage identification. This includes advanced deep learning techniques employing autoencoder neural networks for comprehensive structural damage identification [14], the application of piezoelectric sensors for dynamic strain monitoring to detect local seismic damage in steel buildings [15], and their use in assessing the health of secondary building components [16]. Moreover, innovative methods are continuously being developed to estimate strain responses in complex structures like steel moment-resisting frames using even limited acceleration data [17]. By continuously monitoring the condition of these structures across various scales and types, potential damage can be detected early, enabling timely intervention and preventing catastrophic failures. The ongoing advancements in sensing technologies and data analysis methods continue to significantly enhance SHM system capabilities across all these diverse applications.

Traditional SHM techniques have been widely employed for decades to assess structural integrity, leveraging various sensor types and analysis approaches. For instance, Acoustic Emission (AE) monitoring, while effective in detecting sudden crack propagation and material damage, often struggles with pinpointing exact damage locations in large structures and can be highly sensitive to ambient noise, making long-term, continuous monitoring challenging for slow-developing damage [18]. Similarly, Modal Analysis, which infers structural changes by monitoring alterations in natural frequencies and mode shapes, provides a global assessment of structural health. However, this approach typically lacks the spatial resolution required to detect localised damage effectively, particularly in early stages, and small changes in global modal parameters can be difficult to attribute to specific damage mechanisms [19,20]. These established methods, while valuable, often face limitations in terms of spatial resolution, data interpretation complexity, and suitability for continuous, long-term monitoring, especially for specific damage indicators such as rebar tension state under service loads. By continuously monitoring the condition of structures, potential damage can be detected early, allowing for timely intervention and preventing catastrophic failures. This proactive approach directly translates into significant economic benefits through optimised maintenance planning, extension of service life, and prevention of costly repairs in real-world applications [21,22].

In the context of SHM over the long run, the system's purpose is to provide up-to-date details on the structure's feasibility to carry out its original function [23,24]. There are three primary phases in the design of an SHM system, which can be classified as data collection, analysis, and actual testing [25].

Metrology 2025, 5, 40 3 of 29

Data gathering or data collection is the most crucial phase of an SHM process because it determines the efficacy of future operations. Actual structures require much time and money to experiment with, and causing damage to existing structures is impractical. Therefore, data collection is generally performed on laboratory-scale equivalents or finite element (FE) models. Furthermore, if FE models are sufficiently precise, an arbitrary number of load situations and damage types can be simulated with less effort, and a significant number of measurements can be extracted. Constitutive models provide a mathematical framework for describing the material's mechanical behaviour. The accuracy of numerical simulation approaches for nonlinear dynamic problems has improved thanks to the recent development of numerical methods and material constitutive models. Consequently, FE-based numerical approaches have been widely used [26]. Due to concrete's complex nonlinear behaviour, selecting an appropriate concrete constitutive model for numerical simulations is difficult. In related investigations, the smeared crack constitutive (SCM) model [27] and the concrete damaged plasticity (CDP) model [28] are used to analyse the behaviour of concrete. While both the CDP and the SCM can simulate RC behaviour in FEA, the CDP model is often preferred due to its ability to deliver more thorough and consistent results [29]. The CDP model has been used in a substantial number of FE assessments for concrete structures due to its acceptable performance [30].

Machine learning (ML) models can be used for health monitoring tasks during the second phase of the SHM process, previously referred to as the analysing phase [31]. Traditional ML algorithms are limited in their ability to interpret raw data in its unprocessed form, demanding the use of feature extraction specialists to discover patterns in the input. DL is a subfield of ML, and when raw data are given to a DL model, the model learns the representation needed for classification or identification in the absence of a human mediator. DL's strength is in its ability to explore and understand high-dimensional, complicated data, which has led to its widespread acceptance in the scientific community. One key benefit of DL approaches is that they operate incrementally to uncover high-level features in the data. Because of this, standard feature extraction and knowledge of the relevant area are no longer necessary. To perform big data analytic tasks like classification and prediction, DL enables the use of relatively simple linear models [32]. Furthermore, the fact that massive amounts of data fuel DL is a significant factor in understanding why it is gaining so much popularity [25,33,34].

ANNs form the foundation of DL algorithms and are neural networks with more than three layers. Biological nervous systems have influenced the development of ANN methods [35]. The ability of an ANN to improve its performance by learning identification from experience is one of its most remarkable characteristics. Consequently, trained networks can be applied to the classification and analysis of new datasets that exhibit similarities to trained datasets. ANNs have the potential to model both linear and nonlinear functions. Therefore, this methodology can address various complex problems whose solutions are challenging by using only standard techniques. These include image processing [36], classification [37], pattern recognition [38,39], control systems [40], and identification [41].

The actual testing of SHM systems relies overly on the sensors' precision and the quantity of experimental data captured. Fibre optic sensors (FOS) are used in civil infrastructures for data capture. When compared to conventional sensors, FOS have a number of benefits, including light weight, dependability, stability, compact size, high sensitivity, resistance to electromagnetic disturbances, lower power consumption, multiplexing capabilities, and a broad bandwidth [42]. DOFS can monitor the fibre's physical variations over a network of fibres, unlike a point sensor, which only measures variations at its location. This makes DOFS cost-effective and suitable for civil infrastructure [9,43–45]. Over time, the fibre optic

Metrology **2025**, 5, 40 4 of 29

sensor networks installed on critical civil constructions produce enormous volumes of raw data (big data) [46,47].

Although FOS and DL have limited shared applications, the following applications were noteworthy: operational status of the continuous welded turnouts [1], the evaluation of prestressed concrete bridge girder performance [48], the prediction of column strain responses in high-rise buildings subjected to wind loading [11], recognising and classifying third-party intrusion (external) [49], and preventing third-party damage to underground municipal pipes [50]. Most of these studies utilise FBGs, and the data to test the SHM models can only be extracted at a specific sensing location. In addition, most of the DL and FOS shared applications based on DOFS are used to assess the safety of pipelines.

To the authors' knowledge, there is limited literature on the application of DL and DOFS to monitor the structural health of RC beams [51]. Therefore, the authors present a novel SHM approach to evaluate the structural health of RC beams, utilising FEA for data generation, DL for analysis, and DOFS for data extraction during testing. This research proposes a novel supervised learning method in which the required SHM training data are produced from optimised CDP-based FE simulations by fitting model data to the experimental conditions. Furthermore, the proposed method was applied to real-world beam sizes and generated data for the DL model by modifying the FE model's parameters.

Furthermore, the authors have improved the flexibility of the SHM system by minimising its dependence on sensor location for accurate predictions. In most RC structures, the concrete has already cracked, but steel reinforcement bars are within their elastic limit under service loads [52]. When an RC member is subjected to extreme tension that exceeds the allowable stress in steel, the member goes into yielding. Therefore, when monitoring the structural health of an RC beam, it is essential to be aware of the tension state of the rebar. Although DOFS can be applied to rebars to measure rebar strain in concrete directly in a laboratory setting, the placement and protection of DOFS-attached rebar sensors are difficult in ongoing construction premises due to the fragile nature of the DOFS. Therefore, it would be more convenient if the sensors could be mounted on the concrete surface after construction.

An innovative SHM technique for RC beams was introduced in this study; it combined DOFS, FEA, and DL to forecast rebar tension state under service loads. Superior accuracy was attained by the DL model throughout training, surpassing 98.75%, and it was further validated on experimental data at 100%. Featuring redundancy and adaptability, both the side and bottom sensors exhibited an accuracy of 100%. Additional investigation is required to validate the efficacy of this SHM method under complex loading conditions, despite the method's potential for practical implementation.

2. Materials and Methods

2.1. DL Methods

Recently, DL has emerged as a powerful tool in SHM due to its exceptional ability to learn complex patterns directly from data. This advancement offers new avenues for structural assessment, particularly with the large and high-dimensional sensor data characteristic of modern monitoring technologies like distributed optical fibre sensors. While traditional machine learning (ML) methods often require extensive manual feature engineering and can struggle with the scalability and complexity of such data, DL models inherently excel at these challenges. Their multi-layered architectures enable automatic feature extraction and the identification of intricate, non-linear patterns directly from raw, high-dimensional inputs, significantly reducing reliance on expert-driven feature selection [53–55].

Metrology **2025**, 5, 40 5 of 29

For instance, in the domain of civil SHM, advanced DL-based approaches have demonstrated superior performance in identifying multiclass damage, localising damage, and predicting severity from voluminous vibration data (specifically, acceleration data collected from accelerometers) compared to conventional machine learning algorithms, particularly when dealing with varying environmental conditions like temperature fluctuations. Such models have been validated using both simulated and field experimental data from bridges [53]. Therefore, DL is uniquely suited for the vast and complex data generated by advanced SHM systems, consistently surpassing traditional ML in pattern recognition and data handling capacity for complex SHM applications [56]. However, despite these advantages, DL models in SHM face key limitations. These include a heavy reliance on large, high-quality labelled datasets, susceptibility to overfitting from noise or insufficient data, challenges with interpretability ('black box' nature is critical for safety-sensitive applications), and potential difficulties in generalising to novel damage or environmental conditions [55]. While excelling in data-driven learning, other methods, such as physicsbased models, offer inherent interpretability and robust extrapolation, especially with scarce data [57].

Supervised DL is the most common technique for DL. For the training of a DL model, a sizeable dataset is needed, and the output must have the proper labels [30]. An objective function is used to determine the error between the actual and anticipated output during the training phase, and the weights are adjusted through backpropagation to decrease the error value. To optimise the objective function, gradient-based approaches (Adamax) are applied [58]. A test set is utilised to assess the model's performance, and the testing procedure assesses the ability to generalise for novel inputs. Figure 1 shows the proposed approach to training the DL model.

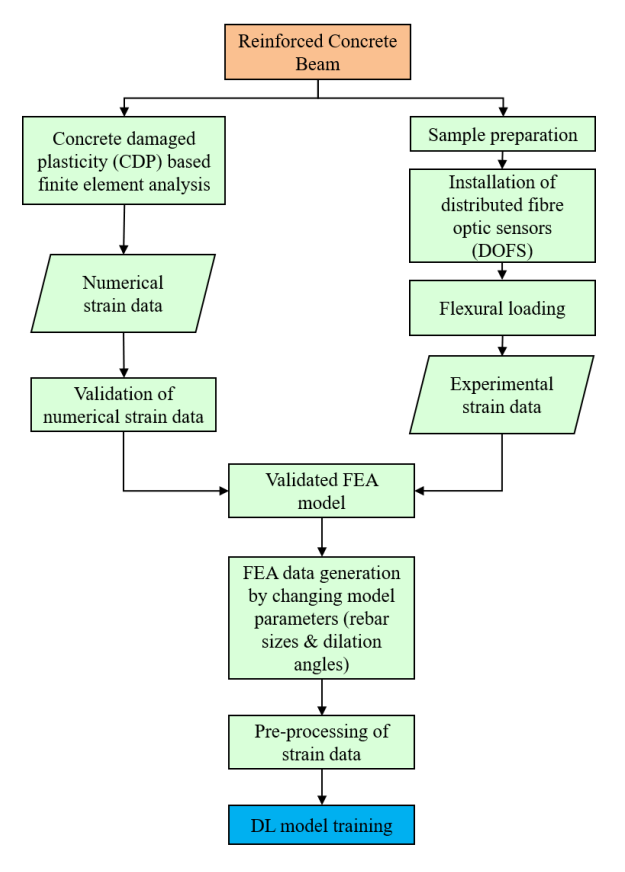


Figure 1. The proposed approach to training the DL model.

Metrology **2025**, 5, 40 6 of 29

2.1.1. ANN Based Framework

An input layer, a hidden layer, and an output layer comprise a neuronal network, which is further connected via training parameters. The primary aim of the ANN is to utilise the concrete surface strain data as input in order to predict the structural integrity of the tension rebar of an RC beam. The determination of the optimal number of hidden layers was based on the complexity of the problem. While ANNs are highly effective with structured numerical inputs, a significant challenge arose from the inherent difference in the number of effective sensor locations (spatial resolution) between the FEA-generated training data and the experimentally acquired DOFS testing data. To address this crucial dimensionality mismatch and ensure a consistent input for the ANN, Principal Component Analysis (PCA) was employed as a robust solution. PCA transforms high-dimensional data into a lower-dimensional representation while preserving underlying trends and patterns [59,60], making it ideal for harmonising data from diverse sources and preparing it for the ANN.

Beyond dimensionality reduction, PCA also offered additional benefits by effectively reducing the inherent redundancy and correlation among adjacent strain measurements along the optical fibre, extracting the most salient features. This improved computational efficiency during ANN training on the large synthetic dataset and helped mitigate overfitting, enhancing model generalisation. While Convolutional Neural Networks (CNNs) excel at spatial feature extraction, their direct application would necessitate a uniform and consistent spatial grid, which was not practically feasible given the inherent differences in data acquisition resolution between FEA and experimental setups. Thus, the combination of PCA for data harmonisation and dimensionality reduction, coupled with an ANN for classification, proved to be an optimal and highly effective solution for our specific problem.

The quantity of variables in the input and output datasets is proportional to the number of input and output nodes in each network. The determination of the optimal number of hidden layers and the number of neurons within each hidden layer was conducted through a systematic trial-and-error approach. This process involved iterative manual exploration of diverse hyperparameter combinations, rather than automated grid or random search. This methodology was chosen for its simplicity and intuitiveness, allowing for a deeper understanding of how specific hyperparameter configurations influence model performance. The 'optimal' configuration was defined as the architecture that consistently achieved the highest validation accuracy while simultaneously preventing overfitting and maintaining high training accuracy. This iterative refinement ensured a robust model performance across both training and unseen validation datasets. The ANN proposed for this study comprised the following: 101 input neurons, 10 neurons in the first hidden layer, 8 neurons in the second hidden layer, and 1 output neuron.

The ANN was compiled using the Adamax optimiser and binary cross-entropy as the loss function. Adamax is a robust variant of the stochastic gradient descent (SGD) algorithm, which iteratively adjusts the network's weights based on the calculated gradients of the loss function. It is particularly effective for deep learning models due to its adaptive learning rate properties, making it suitable for handling the large datasets encountered in our study. The binary cross-entropy loss function was chosen as it is the standard and most appropriate error function for binary classification problems like this, where the model predicts between two discrete outcomes: 'rebar tension not exceeded' and 'rebar tension exceeded'.

The objective of minimising this binary cross-entropy error function is paramount in the context of SHM. A lower error signifies that the model's predicted rebar tension state is in close agreement with the true (labelled) state from our FEA data. In practical SHM applications, accurately predicting whether a critical rebar tension limit has been exceeded Metrology **2025**, 5, 40 7 of 29

directly corresponds to identifying potential structural damage or performance degradation. Therefore, the successful minimisation of this error function ensures the reliability and effectiveness of our deep learning model in providing accurate early warnings for proactive structural assessment and intervention.

It is important to note that the raw strain data obtained from the FEA exhibited a class imbalance between the 'tension not exceeded' and 'tension exceeded' states. To address this challenge and ensure that the deep learning model did not bias its predictions towards the majority class, the SMOTETomek technique was applied as a preprocessing step to the training dataset. SMOTETomek combines the Synthetic Minority Over-sampling Technique (SMOTE) with Tomek links to both oversample the minority class and clean up the majority class examples, thereby balancing the class distribution and promoting more robust and unbiased model learning during the training phase [61,62].

The selection of a fully connected ANN for this classification task was primarily based on its proven capability for handling high-dimensional numerical inputs, its relative architectural simplicity, and its demonstrated computational efficiency [63,64]. For the specific objective of classifying the rebar tension state from the principal components extracted from the strain data, an ANN offered an optimal balance of model complexity and predictive power. While more intricate deep learning architectures might be considered for processing raw spatial or sequential data (e.g., Convolutional Neural Networks or Recurrent Neural Networks), the fully connected ANN, leveraging the effective dimensionality reduction performed by PCA, provided a highly effective and computationally less demanding solution for the defined problem [65]. This approach allowed for rapid training on the large synthetic dataset while maintaining exceptional predictive accuracy for both validation and experimental testing data. The direct nature of the classification problem, involving the transformation of pre-processed strain features into a binary tension state, made the ANN a highly suitable and efficient choice, achieving convincing modelling effectiveness with optimised resource consumption.

2.1.2. ANN Training

In an ANN, all of the nodes in one layer are connected to all of the nodes in the following layer. Only after training with a remaining collection of input–output datasets can an ANN be deployed for predictions. The backpropagation supervised learning algorithm was employed to train the Artificial Neural Network. In essence, backpropagation is the core mechanism by which the network learns from its errors. It involves two main phases: first, the input data is fed forward through the network to generate a prediction. Then, the difference between this prediction and the actual target value (the 'error') is calculated. This error is then propagated backward through the network, layer by layer, to adjust the weights of each connection. The iterative process of adjusting weights based on the error gradient ensures that the network continuously refines its understanding of the input–output relationships, effectively minimising the prediction error.

In the context of SHM, the minimisation of this error through backpropagation is paramount. By constantly adjusting the network's weights to reduce discrepancies between predicted and actual rebar tension states, backpropagation enables our model to accurately identify critical strain conditions. This direct link between error minimisation and precise structural state prediction is fundamental to achieving reliable damage assessment and providing timely warnings for maintenance and intervention in real-world structures.

In technical terms, this is known as backpropagation via gradient descent. To minimise the output error, the error derivative is utilised to alter the weights [66]. Figure 2 shows a typical ANN topology.

Metrology **2025**, 5, 40 8 of 29

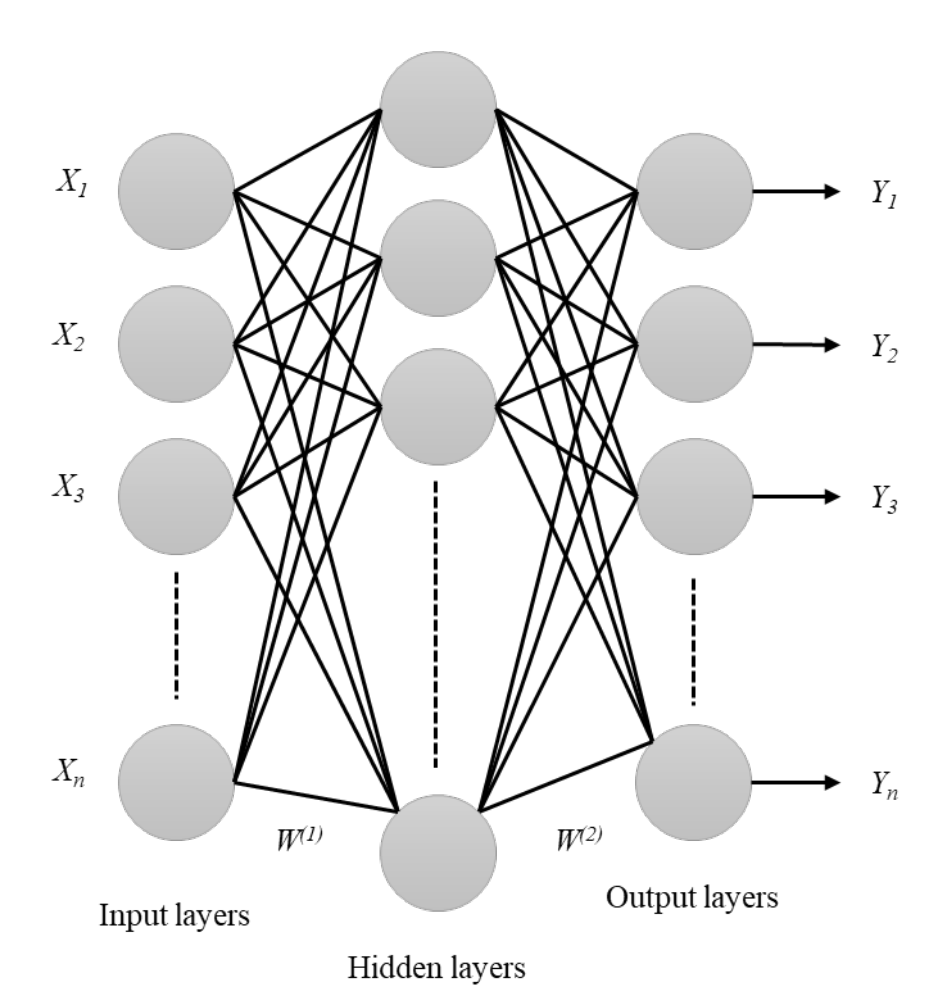


Figure 2. Typical ANN topology.

At the end of the forward pass, the error function corresponding to the weight W is calculated as shown in Equation (1).

$$E(W) = \frac{1}{2} \sum_{k=1}^{k=n} |Y_k - \hat{Y}_k|^2$$
 (1)

where

$$X = [X_1, X_2, \dots X_n]$$
 = Input Vector $Y = [Y_1, Y_2, \dots Y_n]$ = Output Vector $\hat{Y} = [\hat{Y}_1, \hat{Y}_2, \dots \hat{Y}_n]$ = ANN's estimated output vector $W = [W^{(1)}, W^{(2)}]$ = Weight matrices vector for Layers 1 and 2

The derivative of the error function is computed in the backwards pass and used to update the weights according to the following equation.

$$W_{ij} = W_{ij} - \alpha \frac{\delta E(W)}{\delta W_{ij}} \tag{2}$$

where α = Learning rate

 W_{ij} = Specific weight connecting the Units i and j.

Random subdivision of the training data into three distinct subsets—training, validation, and testing—is utilised to ascertain the proportion between the training set and the testing set in the paper. Datasets are typically partitioned into ranges of 5% to 20% for testing, 60% to 90% for training, and 5% to 20% for validation, in accordance with established machine learning practices [67–71]. This allocation of data into these subsets

Metrology **2025**, 5, 40 9 of 29

adheres to this standard procedure. A subset of the data was allocated as follows for the purposes of this study: 64% was designated for training, 16% for validation, and 20% for testing. As the activation function, the ReLU is employed between the initial three adjacent layers, while the sigmoid function is utilised between the last two layers. The ANN architecture is a sequential model with an input layer (101 neurons), two hidden layers (10 and 8 neurons, both with ReLU activation and 'the uniform' initialisation), and a single-neuron output layer (sigmoid activation, 'glorot_uniform' initialisation) for binary classification. Hyperparameters were empirically tuned for optimal performance. The ANN was compiled with the 'Adamax' optimiser, 'binary_cross-entropy' loss, and 'accuracy' metric. Training involved 100 epochs with a batch size of 200, utilising a validation_split of 0.20 to monitor performance and prevent overfitting. Noise treatment involved preprocessing strain data with Quantiletransformer (outputting a normal distribution) to handle non-Gaussian data and outliers. By utilising this methodology, the efficacy of the model was effectively optimised.

Various performance indicators can be used in classification tasks, but no single metric is comprehensively instructive. Therefore, this investigation used accuracy (the percentage of correctly classified observations), precision, and recall to demonstrate the model performance for each case. The percentage of correctly anticipated positive outcomes (true positives) divided by the total number of positive outcomes projected is how precision is computed. The percentage of positives that were accurately identified as such (true positives) divided by the total number of positives yields recall, a metric of completeness.

2.2. Materials and Experimental Methods

2.2.1. Specimen Geometry and Materials

The casting process produced three beams, each of which was 4000 mm long and had a cross section that measured 200 mm by 400 mm. Rebars measuring 12 mm in diameter were used to reinforce each beam's top (compression side). Rebars measuring 12 mm, 16 mm, and 20 mm were used to reinforce the bottom of each beam (tension side). The beam definitions are shown in Figure 3. A 30 mm concrete cover was maintained for all beams. The beams were cast with a Grade 25 concrete premix and kept in wet conditions for seven days. The experimentally measured characteristic cylinder compressive strength (Fck) of the concrete was 29.9 MPa. The RC beams were named R12C30, R16C30, and R20C30 according to the tension rebar sizes of 12 mm, 16 mm, and 20 mm, respectively. All beams maintained a 30 mm concrete covering. The beam was designed according to the European community code EN 1992-1-1: Eurocode 2: Design of concrete structures. All dimensions are in mm.

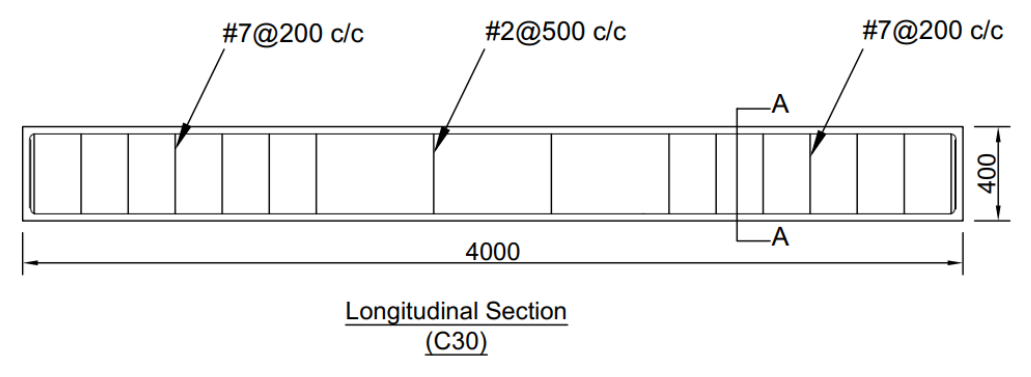


Figure 3. Cont.

Metrology **2025**, 5, 40 10 of 29

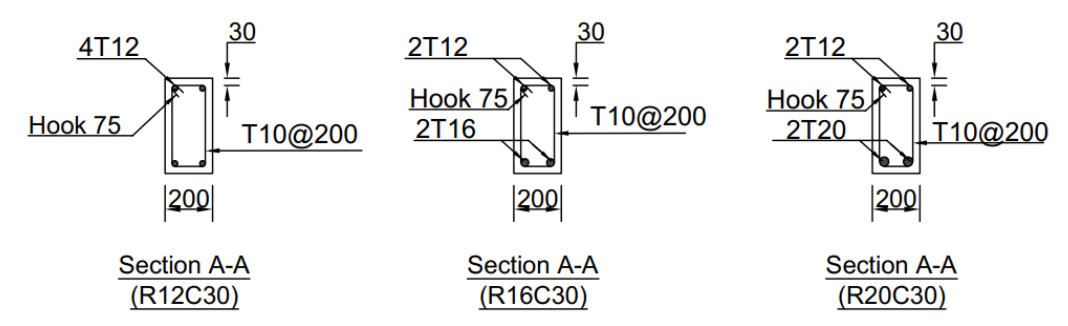


Figure 3. Beam definitions.

2.2.2. Sensor Installation and Strain Monitoring

Strain measurements were taken using an SMF-28 optical fibre. The concrete surface sensor was divided into two segments: the side sensor and the bottom sensor. Two types of epoxy glues were used to mount the rebar and surface sensors. The surface-mounted sensor length was limited to 3000 mm for ease of beam handling (see Figure 4). A slot was ground in a tension rebar using an angle grinder to accommodate the rebar sensors. The fibre is positioned on the rebar so that it faces the bottom of the beam in order to detect the maximum strain.

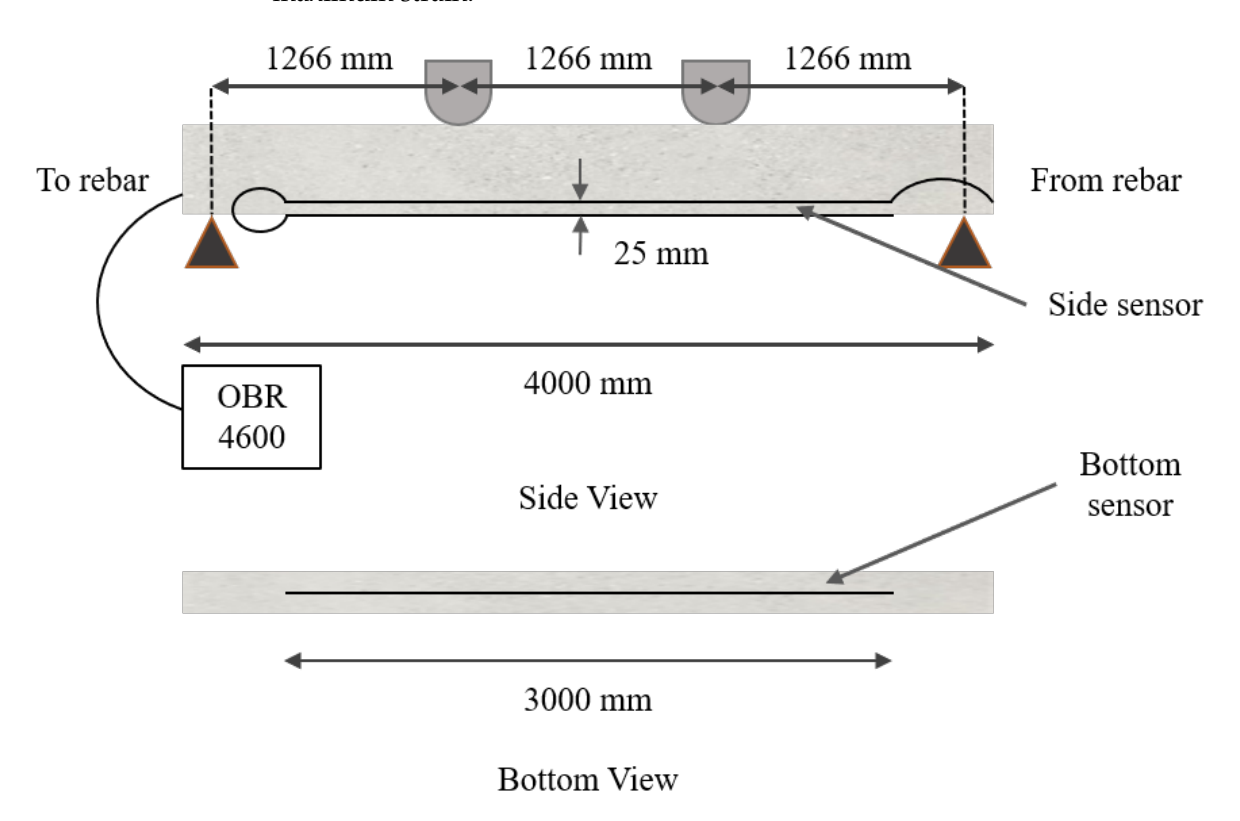


Figure 4. Surface sensor layout.

Figure 4 displays the surface sensor layout, and Figure 5 shows the attached surface and rebar sensors. During the flexural testing, a variation in strain along the surfaces and rebars was monitored and recorded using an OBR 4600. The sensor gauge length and sensor spacing were selected as 2.5 cm and 1 cm, respectively, using the OBR 4600 software, Version 3.10.1.

Metrology **2025**, 5, 40 11 of 29

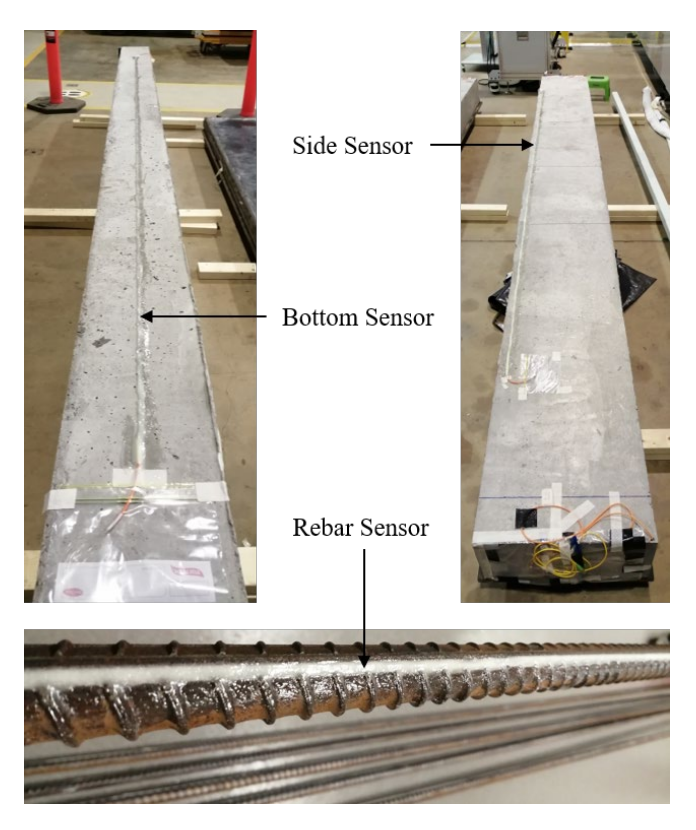


Figure 5. Attached surface sensors and rebar sensors.

2.2.3. Loading Setup

The beams were tested using a hydraulically powered load frame with a 50-tonne capacity. A four-point bending configuration was used for the loading, and all beams were simply supported with a supporting span of 3800 mm. The beam loading configuration is shown in Figure 6, and the loading was maintained until failure occurred. The beams R12C30, R16C30, and R20C30 were loaded up to 60 kN, 120 kN, and 160 kN, respectively, and the readings were recorded at every 10 kN interval.

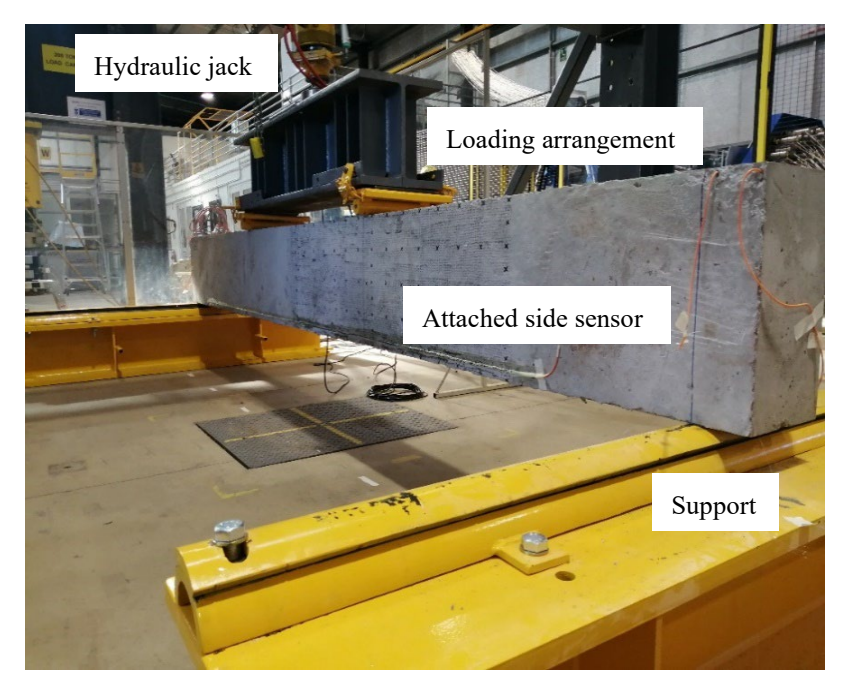


Figure 6. Beam loading arrangement.

Metrology **2025**, 5, 40 12 of 29

2.3. Finite Element Methods

Finite element (FE) analyses of reinforced concrete beams were performed using commercially available software packages. The FE analysis was conducted using ABAQUS/Explicit Version 2019. Strong discontinuities in the geometry or material properties are better suited to an explicit analysis, as it has a higher probability of numerical convergence [72]. The model's accuracy for estimating stress, strain, and displacements should be within acceptable limits. The selection of the CDP model for concrete behaviour was made after careful consideration of various constitutive models, including the Smeared Crack Method (SCM).

The SCM, while capable of considering variables like bond, fracture energy, and mesh size, and effective in predicting maximum crack width in certain engineering applications [73,74], exhibits notable limitations. Its shortcomings become apparent when attempting to predict the maximum to mean crack width ratio, likely due to concrete's inherent heterogeneity [75]. Furthermore, despite its computational efficiency, SCM may face convergence problems stemming from cracking and strain localisation [76] and can suffer from mesh-dependency issues where results depend on element size and orientation [77]. Despite these limitations, the SCM remains a valuable tool for simulating concrete and other material behaviour in numerous structural engineering applications.

In contrast, the CDP model is a more complex yet powerful material model designed to effectively represent concrete's intricate, nonlinear behaviour under load [28]. Founded on a combination of continuum damage mechanics and plasticity theory, it comprehensively accounts for both plastic deformation and damage evolution [78]. Although both the CDP model and SCM can simulate the behaviour of RC in FEA, the CDP model frequently provides more comprehensive and reliable results, making it the preferred choice in many situations, particularly for SHM applications [29]. A key advantage of the CDP model lies in its ability to precisely represent both damage initiation/evolution and plasticity in concrete, capturing the entire nonlinear response, including both cracking and plastic deformation [29]. Therefore, considering its superior capability to capture complex concrete behaviour crucial for accurate SHM simulations, the CDP model was selected for this study.

2.3.1. Finite Element Modelling

Standard 8-node linear brick elements (C3D8R) were used to model the concrete as a solid, homogeneous material using reduced integration and hourglass control. Utilising this element type prevents shear lockup [76,79]. The stirrups and rebars were modelled using the truss elements (T3D2), and truss elements only support compressive or tensile loads. Hexahedral elements (C3D8R) were used to simulate the proposed loading configuration that mimics the experimental loading. The quantity and type of elements utilised in the model were 22156–C3D8R and 1512–T3D2. For modelling simplicity, the constraint among the reinforcement and the beam was modelled using the embedded region function of ABAQUS.

The analysis assumed a perfect interaction between the reinforcement cage and the concrete. A hard contact was used as the contact interaction property for the concrete beam and the loading arrangement in the normal behaviour, while a friction coefficient of 0.3 was used for the tangential behaviour [80]. Material properties of concrete stress-strain data for tensile and compressive behaviour, and the damage parameters for tension and compression, were calculated using the CEB-FIP model code 1990 [81]. Table 1 summarises the properties of concrete and steel.

Metrology **2025**, 5, 40

Table 1. Concrete and steel properties.

Material	Type	Young's Modulus (MPa)	Poisson's Ratio
Concrete	Isotropic	27,106	0.2
Steel	Isotropic	200,000	0.3

2.3.2. Concrete Damaged Plasticity (CDP) Model

CDP is a widely established model for simulating the nonlinear behaviour of RC [80,82]. The CDP model includes concrete's plastic, compressive, and tensile behaviours, and concrete is assumed to be homogeneous, isotropic, and continuous [83]. The primary parameters considered in this study were flow potential eccentricity (ϵ), dilation angle (ψ) , the ratio of the compressive strength under biaxial loading to uniaxial compressive strength (fb0/fc), shape factor (K), viscosity parameter (μ), elasticity modulus of concrete (Ec), and density. It should be noted that a viscosity parameter was not utilised because ABAQUS/Explicit was used for the simulation; hence, its value was assumed to be 0 [84]. The CDP model was validated for the R20C30, and the R12C30 and R16C30 beams were kept for use in the prediction stage. Table 2 summarizes the optimal dilation angle and other CDP parameters for the R20C30 beam. Mesh sizes smaller than 25 mm were not considered because the aggregate size was 20 mm. A convergence study was conducted utilising 50 mm, 40 mm, 30 mm, and 25 mm mesh sizes. The investigation for mesh size selection revealed that using the mesh size of 25 mm yields the most realistic modelling of the observed behaviour. Only 4.2% variation was observed when compared to the R20C30 beam displacement at failure load; therefore, FEA was performed using a 25 mm mesh.

Table 2. CDP properties for the R20C30 beam.

Beam No.	Dilation Angle	Eccentricity	f_{b0}/f_{c0}	K	Viscosity Parameter
R20C30	43°	0.1	1.16	0.667	0

2.3.3. Synthetic Strain Data Generation

The amount of training data used to train a DL model determines its precision. The dilatational angle is a very important parameter in the CDP model. For lesser values, the material is brittle, while for higher values, it is stiffer. Typically, the dilatation angle of concrete ranges from 13° to 56° [82]. In this work, strain data was generated by a series of simulations in which the dilation angle was varied from 31° to 45° (with an increment of 1°). The change in dilatation angle led to generalising the training data from brittle to stiffer conditions. The field output request interval was adjusted to 2500 at a frequency of evenly spaced time intervals for each simulation, and the CDP model loaded until the rebar yields. Therefore, the surface and rebar data can be extracted until the elastic limit ends. Along the sensor path for each sensor, 37500 data points can be extracted using this method for each beam definition. The varied CDP model parameters to generate strain data are tabulated in Table 3.

In this study, the strain retrieved along the surface sensor path from the FEA model was the input data, and the output was the rebar status indicating whether or not a predefined rebar strain was exceeded. Here, in the proposed ANN, the output node is adopted in the output layer, where the value "1" means that the limit was exceeded, and "0" indicates that the limit was not exceeded. The model was trained to predict the rebar tension statuses, from 10% to 90%, in 10% steps by considering the rebar yield limit (yield strain of steel considered 2500 $\mu\epsilon$).

Metrology **2025**, 5, 40 14 of 29

Rebar Size (mm)	Dilation Angle (°)	Steps	Number of Data Points per Each Sensor (No of Dilation Angles \times Steps)
12	210 to 450		37,500
16	31° to 45° (15 angles)	2500	37,500
20			37,500
Total no. of data for eac	h sensor		112,500
Total number of data us (Bottom sensor + Side s			225,000

Table 3. CDP model parameters for strain data generation.

It is important to acknowledge that while FEA provides a controlled and detailed dataset for training and validating the deep learning model, an inherent limitation lies in the potential for overfitting or biasing the model towards idealised simulation conditions. FEA models, by nature, simplify real-world complexities such as material inhomogeneities, exact boundary conditions, and unforeseen loading irregularities. Consequently, this reliance on simulated data might, to some extent, limit the model's generalisation capability when exposed to the full spectrum of real-world variations or highly complex loading scenarios. Validating the model's performance under a wider array of real-world conditions, including diverse material properties, environmental effects, and dynamic loading, warrants additional investigation. This is a crucial step towards ensuring the robustness and practical applicability of the proposed SHM approach.

3. Results and Discussion

This section presents and discusses the analysis of the DOFS and FEA rebar strain results, the analysis of DOFS and FEA surface strain results, and DL predictions. Even though ultimate load testing was performed on the beams, the data reported here are based only on the sensor readings' spectral shift quality (SSQ). The manufacturer of the data acquisition system (OBR 4600) states that the SSQ quantifies the correlation between the measured and reference reflected spectra [85]. SSQ values can be calculated using the following expression:

$$Spectral\ Shift\ Quality(SSQ) = \frac{MAXIMUM(U_j(v) \star U_j(v-v_j))}{\sum U_i(v)^2} \tag{3}$$

 $U_i(v)$ = Baseline spectrum for a given data segment

 $U_j(v-v_j)$ = The spectrum measured during a strain or temperature change

 \star = The symbol represents the cross-correlation operator.

Theoretically, the SSQ should have a value between 0 and 1, with 1 indicating perfect correlation and 0 indicating no correlation. The manufacturer recommends disregarding data with a spectral shift quality (SSQ) equal to or less than 0.15, as this threshold indicates that the strain or temperature variation has unequivocally exceeded the measurable range. Consequently, measurements falling below this SSQ threshold were excluded. Despite this initial filtering, other strain reading anomalies, such as implausible high- or low-value strain spikes, were still observed in the data [31]. Such inconsistencies in optical fibre sensor measurements have also been reported in existing literature [86,87]. Therefore, anomalous data points were identified using scatter plots and removed from the dataset.

The removal of these anomalies is crucial because their presence would directly lead to unreliable outcomes. Anomalous data points, such as those with poor SSQ, do not represent the true strain state of the reinforced concrete beam and, if retained, would Metrology **2025**, 5, 40 15 of 29

introduce significant errors into the FEA model validation process and distort the testing data for the deep learning model. This would ultimately undermine the accuracy and reliability of the model's predictions regarding rebar tension states, potentially leading to incorrect structural health assessments and flawed maintenance decisions.

Experimental observations indicated that the SSQ values of the rebar were within an acceptable range until 80% of the elastic strain limit (2000 $\mu\epsilon$). The bottom surface sensor first reached the 0.15 SSQ threshold, followed by the side sensor for all three beams. The data presented in this section depend purely on the side surface sensors' maximum load, which could be reached for the beams R20C30, R16C30, and R12C30 before dropping below the 0.15 SSQ limit: 60 kN, 40 kN, and 20 kN, respectively. Table 4 illustrates the effect of SSQ on beams R12C30, R16C30 and R20C30.

	R12C30		R16C30		R20C30	
Load (kN)	Bottom Sensor	Side Sensor	Bottom Sensor	Side Sensor	Bottom Sensor	Side Sensor
10	CCO - 0.15					
20	SSQ > 0.15		SSQ > 0.15		000 015	
30				SSQ > 0.15	SSQ > 0.15	SSQ > 0.15
40	$SSQ \le 0.15$					33Q > 0.13
50			000 < 0.15		$SSQ \le 0.15$	•
60			$SSQ \le 0.15$	$\text{SSQ} \leq 0.15$		
70						SSQ < 0.15

Table 4. Effect of SSQ on beams R12C30, R16C30, and R20C30.

3.1. Analysis of DOFS and FEA Rebar Strain Results

Figure 7 illustrates the strain measurements from the experiment and simulation along the rebar for the beam R20C30 under two distinct load circumstances, including 40 kN and 60 kN. Both experimental and simulated strain patterns exhibited excellent correlation. At a load of 60 kN, the maximum rebar strain was measured as 992 $\mu\epsilon$.

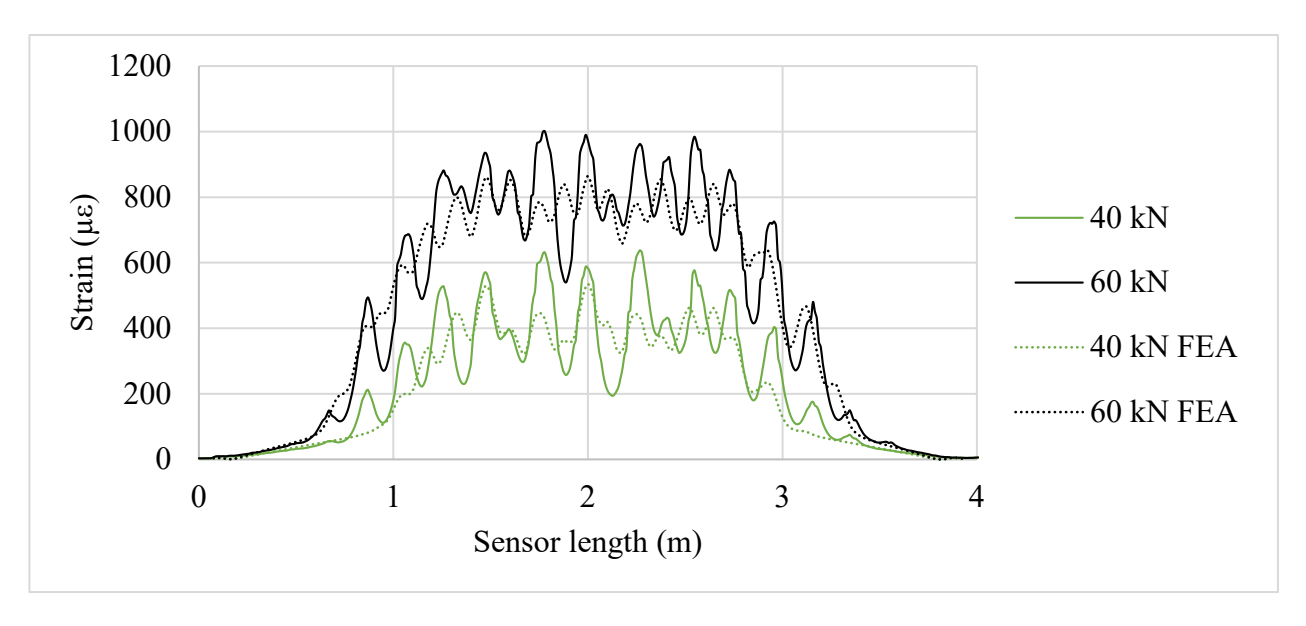
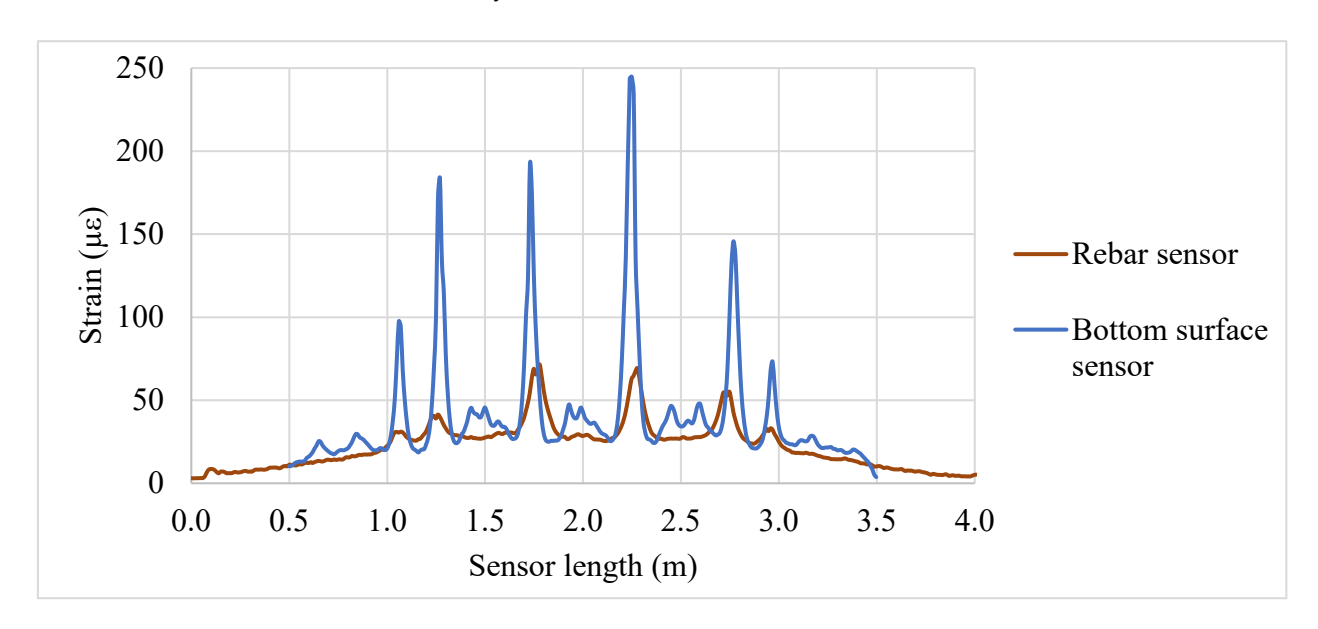


Figure 7. Experimental vs. simulation rebar strain for beam R20C30.

Strain peaks in the rebar exhibit a wavey behaviour for all measurements, and this wavy behaviour is amplified as the load increases. This resulted from the crack propagating

Metrology **2025**, 5, 40 16 of 29

along the longitudinal direction of the beam. Figure 8 explains this trend in greater detail. The illustration presents the fluctuation in the strain result for the bottom surface sensor and rebar sensor under a 10 kN load for the beam R20C30. Examining the graph, it is evident that the rebar strain spikes correspond with the surface strain peaks. In DOFS measurements, the appearance of distinct strain peaks serves as a direct indicator of crack formation induced by tension at that corresponding location. This phenomenon arises because as a crack opens and propagates, the optical fibre spanning the crack experiences a sharp localisation and amplification of tensile strain. Conversely, strain valleys within the profile typically correspond to areas where the concrete is subjected to lower strain levels. As the surface strain spikes result from crack formation, so do the rebar strain spikes. Therefore, it can be deduced that the rebar strain peaks are caused by the concrete cracks that traverse beyond the rebars.



 $\textbf{Figure 8.} \ Strain\ variation\ of\ the\ rebar\ and\ bottom\ surface\ sensor\ under\ a\ 10\ kN\ load\ for\ beam\ R20C30.$

This phenomenon holds significant implications for SHM applications. Firstly, the strain peaks serve as a clear and quantifiable fingerprint of damage initiation and progression within the reinforced concrete beam. Secondly, the strong correlation between surface and internal (rebar) strain peaks is crucial, validating the use of surface-mounted DOFS to infer the critical internal tension state of the rebar. This is particularly advantageous in real-world scenarios where direct rebar sensor installation and protection can be challenging due to the fragile nature of DOFS and ongoing construction activities.

The difference between the maximum experimental and simulation strains was 128 $\mu\epsilon$ under a 60 kN load. The maximum simulation rebar strain was 864 $\mu\epsilon$. This is because the wavy behaviour was significantly more pronounced in the experimental strain data than in the simulation results for all readings.

3.2. Analysis of DOFS and FEA Surface Strain Results

Figure 9 displays the strain measurements from the experiment and simulation along the bottom surface sensor length of the R20C30 beam at 40 kN. The maximum experimental strain measured was 3557 $\mu\epsilon$, while the simulation peak strain was measured as 2811 $\mu\epsilon$. Figure 10a,b shows the experimental and simulation strain variation in the side surface along the sensor length of beam R20C30 at 40 kN and 60 kN, respectively. Under a load of 60 kN, the maximum strain measured experimentally was 5614 $\mu\epsilon$, while the maximum

Metrology **2025**, 5, 40 17 of 29

strain recorded in simulations was 4753 $\mu\epsilon$. This surface sensor was positioned 25 mm above the bottom surface of a concrete beam wall.

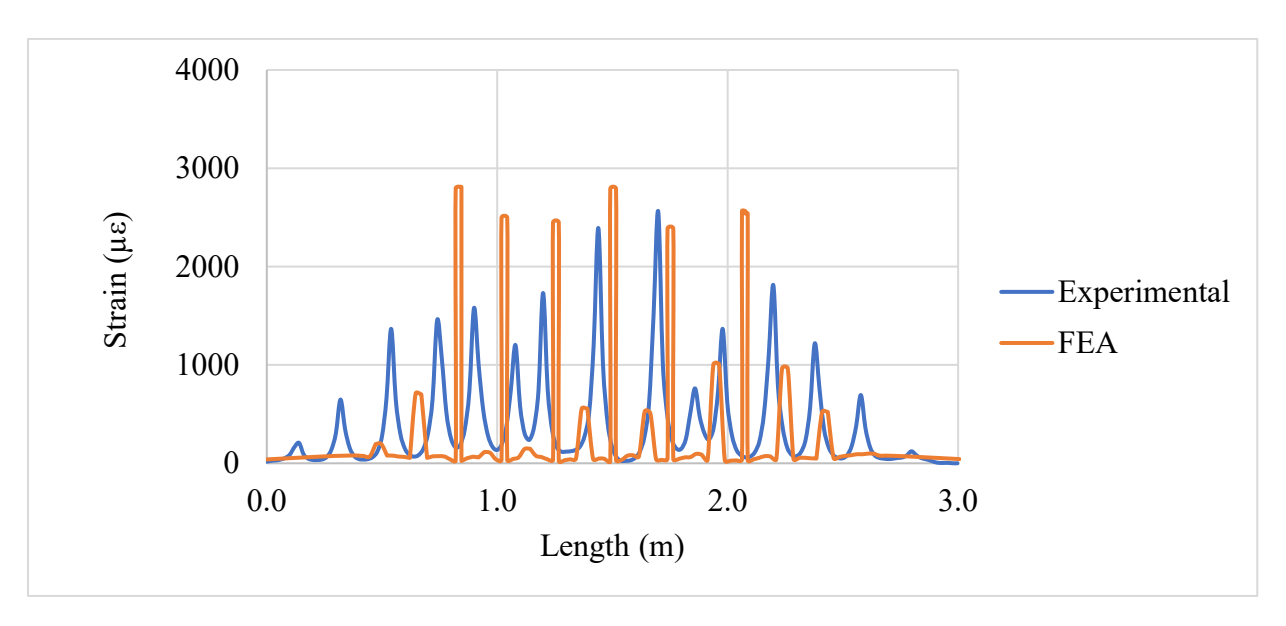


Figure 9. Experimental vs. simulation bottom surface strain for beam R20C30 at 40 kN.

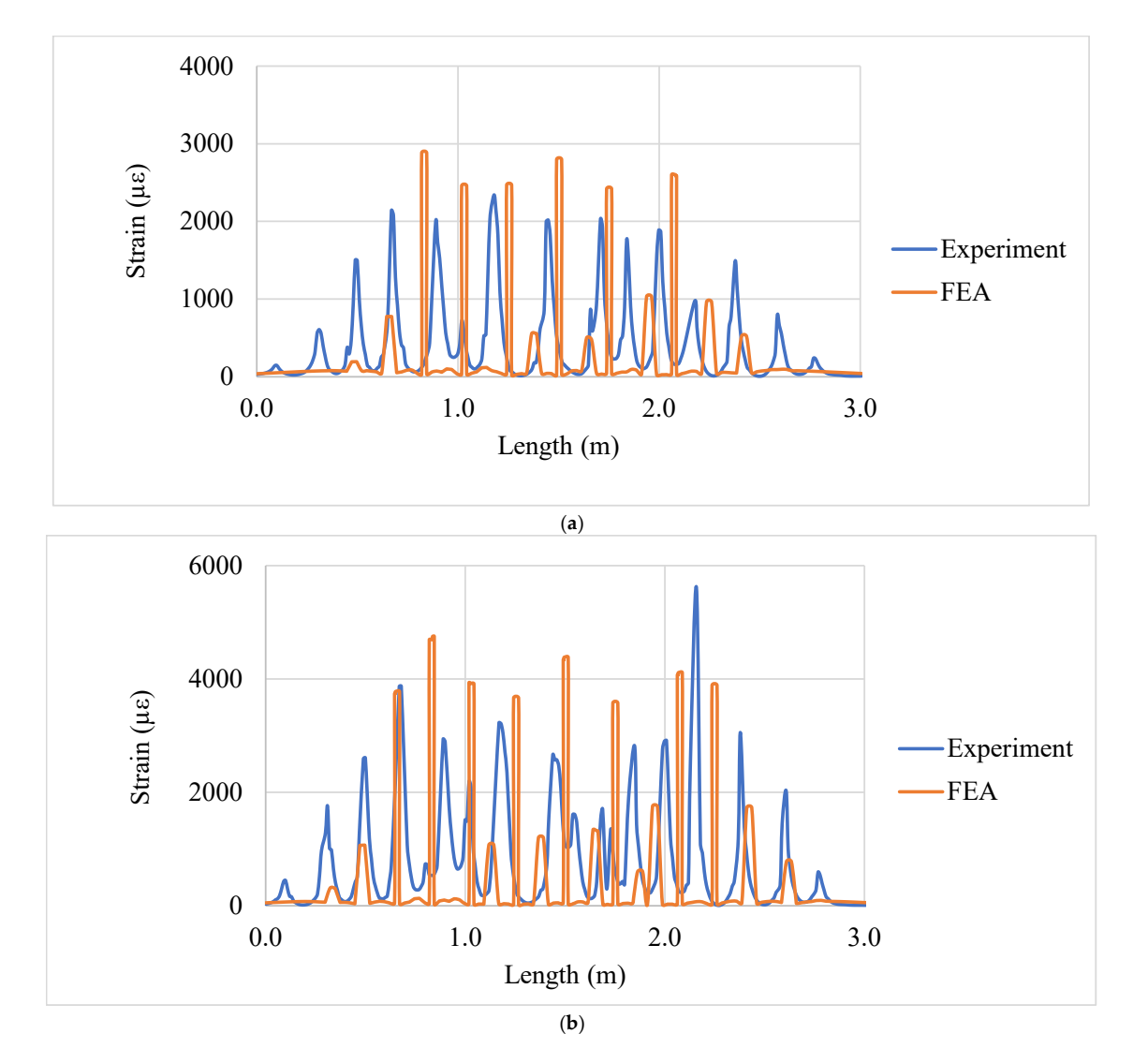


Figure 10. Experimental vs. simulation side surface strain for beam R20C30 (a) at 40 kN and (b) at 60 kN.

Metrology **2025**, 5, 40 18 of 29

Figure 10 shows a progressive increase in the amplitude and number of strain peaks as the load increased. This is due to the onset of cracks and the widths of the cracks increasing with the increasing load. Furthermore, the progressive increase in the amplitude and number of strain peaks with increasing loads (Figures 9 and 10) provides valuable insight into the evolution of crack widths and overall structural degradation. Capturing and analysing these crack-induced strain patterns is fundamental for training and validating robust SHM systems, especially those leveraging deep learning. Our developed model is designed to effectively handle these peaks generated by cracks on the surface, thereby enhancing its robustness for health prediction across a wider range of RC concrete beams. By considering Figures 9 and 10, both the bottom and the side surfaces were substantially cracked for the loads presented. Strain peaks are visible from the very beginning to the very end of the sensor length.

The experimental and simulated crack positions and the strain magnitude along the length of the beam exhibit notable differences, which could be attributable to various reasons. To begin with, it is conceivable that the presence of small cracks on the surface of the concrete material, caused by the shrinkage process during its casting, may have been a contributing factor. Additionally, errors in misalignment that occurred during testing, as well as any damage sustained during the lifting of the specimens, could also have played a role. Lastly, it is important to note that in practical construction settings, imperfections such as uneven compaction of concrete, misalignment of reinforcement, or variations in cross-sectional dimensions may also be present. While these factors can impact experimental results, on the other hand, the default CDP model's isotropic nature may limit its ability to accurately predict complex anisotropic cracking patterns. However, the number of peak strains and overall pattern in the experiment and simulation were in admissible agreement. After examining Figure 9, the experiment yielded a total of 14 instances of peak strain values, whereas the FEA revealed 13 instances of peak strains. In Figure 10a, a comparison between the experimental and FEA results indicates a total of 15 peak strains in the experimental data and 13 peak strains in the FEA data. In Figure 10b, the experimental data recorded 17 instances of peak strains, which is consistent with the 17 instances of peak strains identified by the FEA analysis. Consequently, the FEA model can be validated by considering strain distribution. The generation of the strain data and DL model training using CDP-based FEA data were performed.

Deep Learning Predictions

The trained DL model's performance indicators are reported in Table 5. Maximum training accuracy, validation accuracy, and precision were 99.76%, 99.77%, and 0.9983, respectively, for the 20% rebar strain limit. The maximum recall for the 30% rebar strain limit was measured at 0.9971. Training and model validation accuracy for all rebar strain limits was greater than 98.66%. To further elaborate on the classification effectiveness of the developed deep learning model, additional visual performance metrics are presented. Figure 11 presents the confusion matrix, providing a detailed breakdown of the model's true positive, true negative, false positive, and false negative predictions for the testing dataset. This matrix clearly illustrates the precise classification accuracy for both 'tension not exceeded' and 'tension exceeded' states across different output percentages (e.g., 10% to 90% of yield). The confusion matrix provides a direct and comprehensive visual assessment of the model's ability to correctly classify each tension state and identify potential misclassifications.

Metrology **2025**, 5, 40

Table 5. Model performance indicators
--

Model Training	Model Performance			
(Rebar Strain Limits)	Training Accuracy (%)	Validation Accuracy (%)	Precision	Recall
10%	99.64	99.63	0.9971	0.9965
20%	99.76	99.77	0.9983	0.9965
30%	99.73	99.70	0.9966	0.9971
40%	99.23	99.24	0.9934	0.9916
50%	99.17	99.14	0.9947	0.9874
60%	99.11	99.10	0.9912	0.9904
70%	98.94	98.84	0.9821	0.9951
80%	98.88	98.83	0.9806	0.9968
90%	98.75	98.66	0.9800	0.9953



Figure 11. Confusion matrix.

The variation in the total number of data points observed across different confusion matrices (e.g., 'Model Training—10%' to 'Model Training—90%') is directly attributed to each matrix being generated on a distinct subset of the overall dataset. These subsets are defined by the 'output percentage' context, meaning each evaluation point corresponds to a specific threshold of rebar tension (e.g., 10% of yield, 20% of yield, etc.). Consequently, as this rebar tension threshold changes for each 'output percentage' subset, the inherent definition of 'rebar tension not exceeded' versus 'rebar tension exceeded' is altered, naturally leading to different total numbers of samples and varying class compositions within each respective subset. As previously discussed, class imbalance in the original dataset

Metrology **2025**, 5, 40 20 of 29

was addressed using SMOTETomek during the model's training phase to ensure robust learning and unbiased evaluation across these varying tension ranges.

After training, the DL model was utilised and programmed to predict the rebar tension state as a class for the experimental result obtained using DOFS. Tables 6 and 7 show the assigned classes for each rebar tension state and guide for prediction, respectively. The experiment results from the bottom sensor and side sensor for the beams R12C30, R16C30, and R20C30 were entered into the DL model, and the results are tabulated in Tables 8–10, respectively.

Table 6. Assigned classes.

Class	Rebar Tension State
Class 0	Rebar is strained within 0–250 με
Class 1	Rebar is strained within 251–500 με
Class 2	Rebar is strained within 501–750 με
Class 3	Rebar is strained within 751–1000 με
Class 4	Rebar is strained within 1001–1250 με
Class 5	Rebar is strained within 1251–1500 με
Class 6	Rebar is strained within 1501–1750 $\mu\epsilon$
Class 7	Rebar is strained within 1751–2000 με
Class 8	Rebar is strained within 2001–2250 $\mu\epsilon$

Table 7. Guide for predictions.

Colour	Description	
	Correct prediction	
	Incorrect prediction	

Table 8. DL model predictions for R12C30.

Load (kN)	Maximum Experimental Rebar Strain (με) in	Rebar Tension State Prediction		
	Input Dataset	Bottom Sensor	Side Sensor	
10	80	Class 0	Class 0	
20	776	Class 3	Class 3	

Table 9. DL model predictions for R16C30.

Load (kN)	Maximum Experimental Rebar Strain (με) In Input Dataset	Rebar Tension State Prediction		
		Bottom Sensor	Side Sensor	
10	74	Class 0	Class 0	
20	267	Class 1	Class 1	
30	645	Class 2	Class 2	
40	994	SSQ < 0.15	Class 3	

Table 10. DL model predictions for R20C30.

Load (kN)	Maximum Experimental Rebar Strain ($\mu\epsilon$) in Input Dataset	Rebar Tension State Prediction		
		Bottom Sensor	Side Sensor	
10	71	Class 0	Class 0	
20	185	Class 0	Class 0	
30	438	Class 1	Class 1	
40	638	Class 2	Class 2	
50	823	— SSO < 0.15	Class 3	
60	992	== 33Q < 0.13	Class 3	

Metrology **2025**, 5, 40 21 of 29

Appendix A provides the graphs of experimental data for the R12C30 and R16C30 beams. The proposed DL model was evaluated with 21 experimental findings in each of the three beams. The DL model predicted 21 correct results out of 21 experimental data points, corresponding to an overall accuracy of 100%.

The results from the bottom and side sensors were independently evaluated in the following stage. The DL model predicted nine correct results out of nine experimental results for the bottom sensor, resulting in an accuracy of 100%, and 12 accurate results out of 12 experimental results for the side sensor, resulting in an accuracy of 100%. Since the prediction accuracy for both sensors was 100%, if one sensor fails, the other can be deployed as a substitute, improving the suggested SHM system's usefulness since the dependence on a single sensor can be eliminated. Even though the accuracy of the bottom sensor was 100%, under increasing loads, the bottom sensor exhibited significantly low SSQ values (below 0.15). This indicated that its measurements became unreliable at higher loads. Consequently, the side sensor was identified as more reliable due to its consistent SSQ with increasing loads when compared to the bottom sensor. This finding is crucial, informing our recommendation for optimal sensor placement on the beam sidewall for robust, long-term structural health assessment in practical applications. Finally, the DL model was updated to predict the maximum rebar strain status as a class when a series of input data was offered to the model to improve robustness. While the proposed deep learning model demonstrated exceptional accuracy in predicting rebar tension states for the experimental data generated in this study, it is important to acknowledge that the validation was based on a limited number of RC beams.

Traditional benchmarks in the domain of SHM for RC beams have been established using vibration-based monitoring, AE monitoring, and ultrasonic testing. The study presents an innovative approach that utilizes the surface strain of concrete as the main input to a deep learning model in order to forecast classifications of rebar strain. This method for SHM in concrete beams has not yet been implemented, resulting in a dearth of direct benchmarks for this technique, as far as the author is aware. One of the main considerations is the practicality of the DL model, which, notwithstanding its remarkable precision, has solely undergone evaluation in controlled experimental environments.

While the experimental validation presented provides crucial insights and confirms the feasibility of the proposed approach, it is acknowledged that the current scope is limited to specific beam sizes and loading regimes. The conducted tests served to demonstrate the fundamental principles of distributed sensing and deep learning for SHM of reinforced concrete beams under controlled laboratory conditions. For future work, broader experimental testing encompassing diverse geometries (e.g., varying beam depths, widths, and span lengths), a wider range of environmental conditions (e.g., temperature fluctuations, humidity), and varied sensor placements would be invaluable. Such comprehensive validation would further solidify the robustness claims of the proposed method and enhance its generalisation capability for real-world structural health assessment applications.

4. Conclusions

In this investigation a novel SHM technique for RC beams is proposed to predict the rebar tension state of a structure under service loads by employing DOFS, FEA, and DL. A validated CDP-based FEA model was used to generate concrete surface and rebar strain data. The generated strain data was used to train a DL model which predicts the structural health of three reinforced concrete beams. The DL model needs only the extracted strain data (SSQ > 0.15 for DOFS) from the bottom or side concrete surface of an RC beam. Furthermore, it automatically handles the peaks created by cracks on the surface, and therefore, the model is robust enough to apply to health prediction for a wider range of RC

Metrology 2025, 5, 40 22 of 29

concrete beams. Finally, the proposed DL model predicts the status of rebar tension as a class, and the following remarks can be drawn at the end of this study:

- 1. The DL model recorded more than 98.75% training and validation accuracy.
- 2. The overall prediction accuracy of the DL model was 100% for the experimental dataset.
- 3. The prediction accuracy of both side and bottom sensors was 100%, and the side sensor could replace the bottom sensor if it were damaged, or vice versa, so decreasing sensor position reliance.
- 4. It is recommended to attach sensors on the beam sidewall compared to the bottom surface due to the low SSQ values (<0.15).

Therefore, the proposed SHM approach can be implemented in real-world structures, and additional research is necessary to determine the accuracy of the predictions under complex operational loading conditions such as the asymmetric loading condition.

Author Contributions: Conceptualization, M.J., N.H., H.S., and J.E.; methodology, M.J., N.H., H.S., and J.E.; software, M.J., and J.E., and B.G.P.; validation, M.J., S.B. and J.E.; formal analysis, M.J., and M.H.; investigation, M.J., and M.H.; data curation, M.J., M.H., and S.B.; writing original draft preparation, M.J., and J.E.; writing review and editing, N.H., H.S., J.E., and B.G.P.; visualization, M.J.; supervision, N.H., H.S., and J.E.; project administration, N.H., H.S., and J.E.; funding acquisition, M.J., and J.E. All authors have read and agreed to the published version of the manuscript.

Funding: This research received no external funding.

Data Availability Statement: The raw data supporting the conclusions of this article will be made available by the authors on request.

Acknowledgments: The first author would like to express gratitude to the University of Southern Queensland, Australia, for funding his doctoral studies through an International Ph.D. fees scholarship. The first author also thanks Uva Wellassa University in Sri Lanka for providing paid leave to complete this project. The authors would also like to extend their appreciation to Janitha Jeewantha, Chris Emmanuel, Sandaruwan Jayalath, Piumika Ariyadasa, Wayne Crowell, and Choman Salih, who all contributed to the beam cast and the experiments.

Conflicts of Interest: The authors declare that they have no known competing financial interests or personal relationships that could have appeared to influence the work reported in this paper.

Appendix A

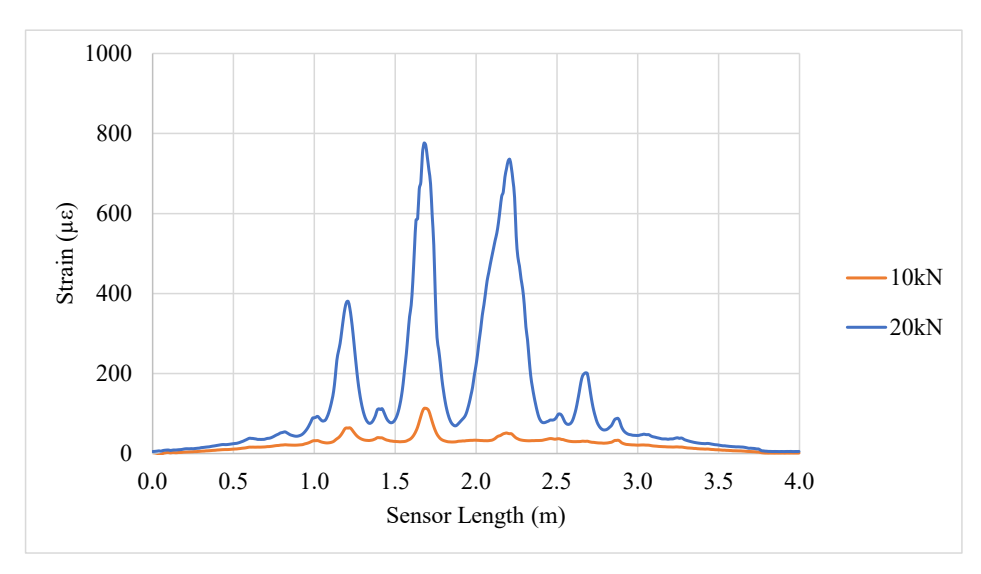


Figure A1. Rebar strain along the sensor length for beam R12C30.

Metrology **2025**, 5, 40 23 of 29

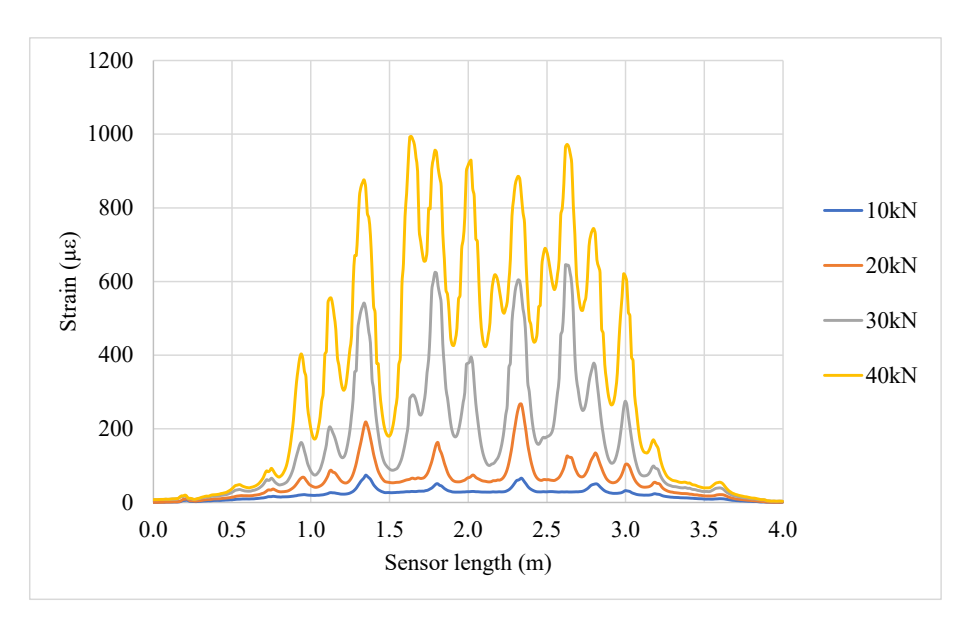


Figure A2. Rebar strain along the sensor length for beam R16C30.

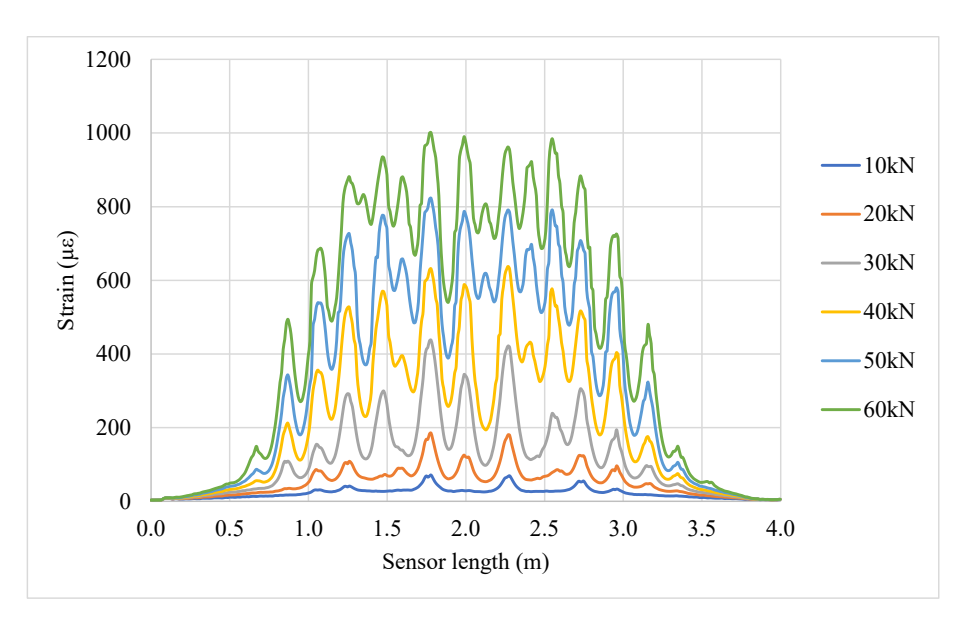


Figure A3. Rebar strain along the sensor length for beam R20C30.

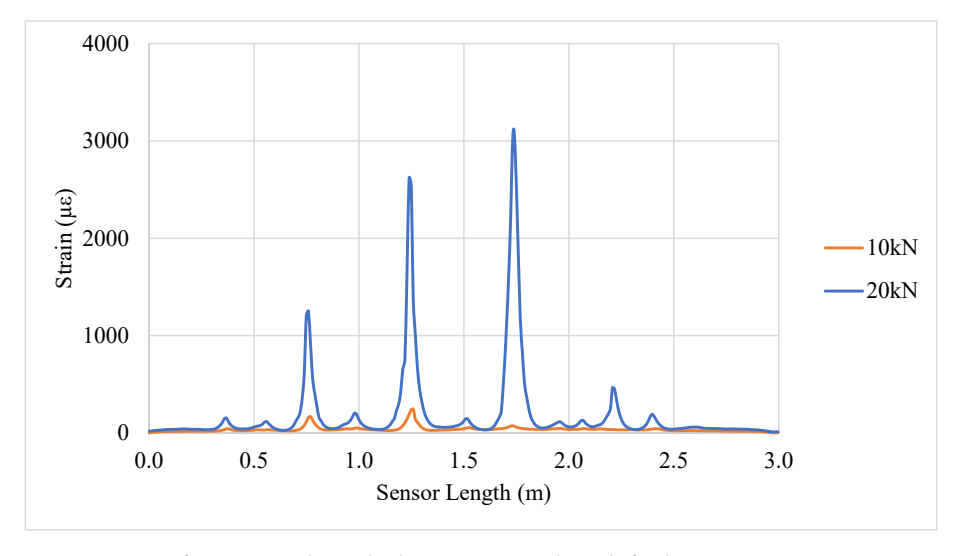


Figure A4. Surface strain along the bottom sensor length for beam R12C30.

Metrology **2025**, 5, 40 24 of 29

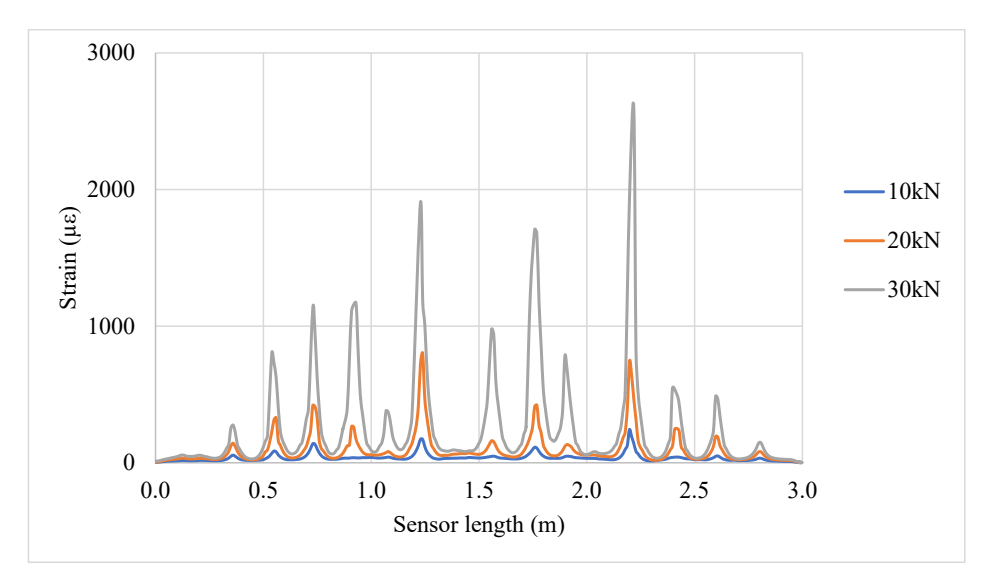
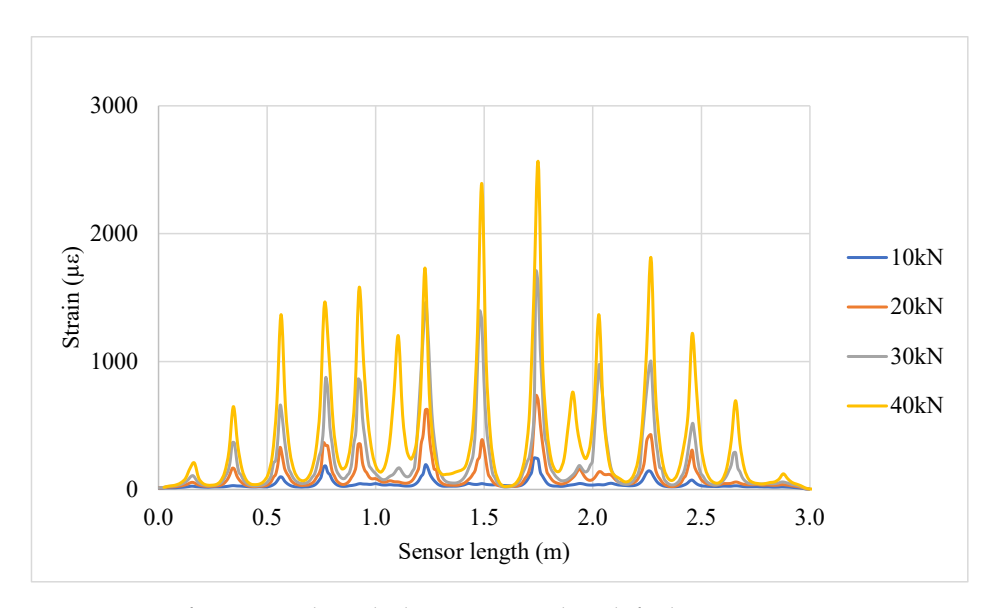


Figure A5. Surface strain along the bottom sensor length for beam R16C30.



 $\label{eq:Figure A6.} Figure \ A6. \ Surface \ strain \ along \ the \ bottom \ sensor \ length \ for \ beam \ R20C30.$

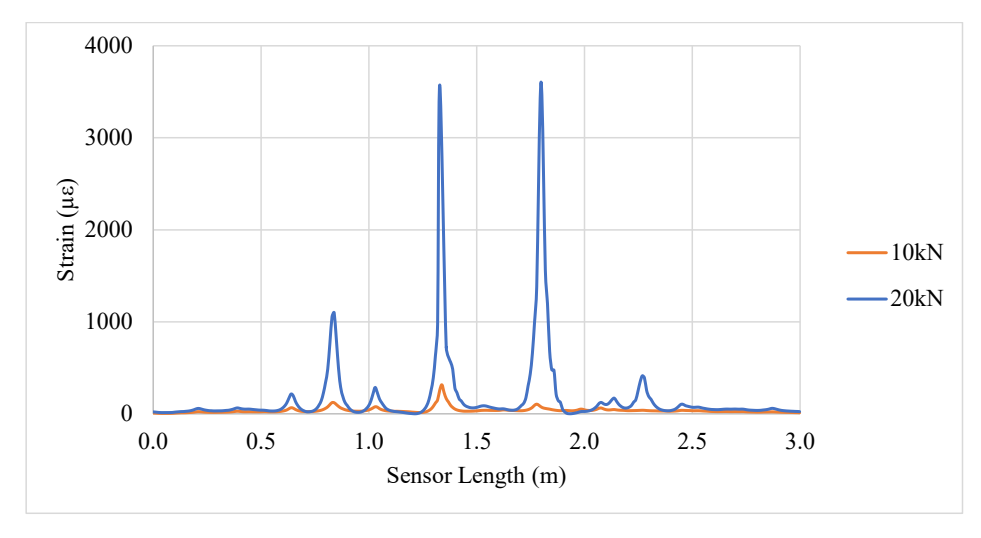


Figure A7. Surface strain along the side sensor length for beam R12C30.

Metrology **2025**, 5, 40 25 of 29

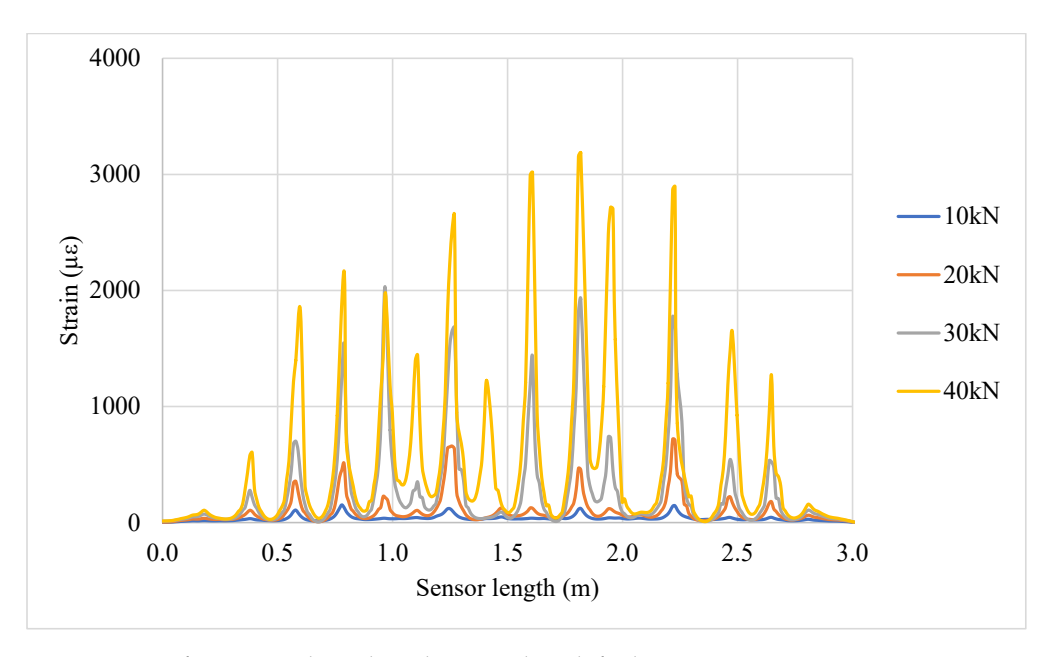


Figure A8. Surface strain along the side sensor length for beam R16C30.

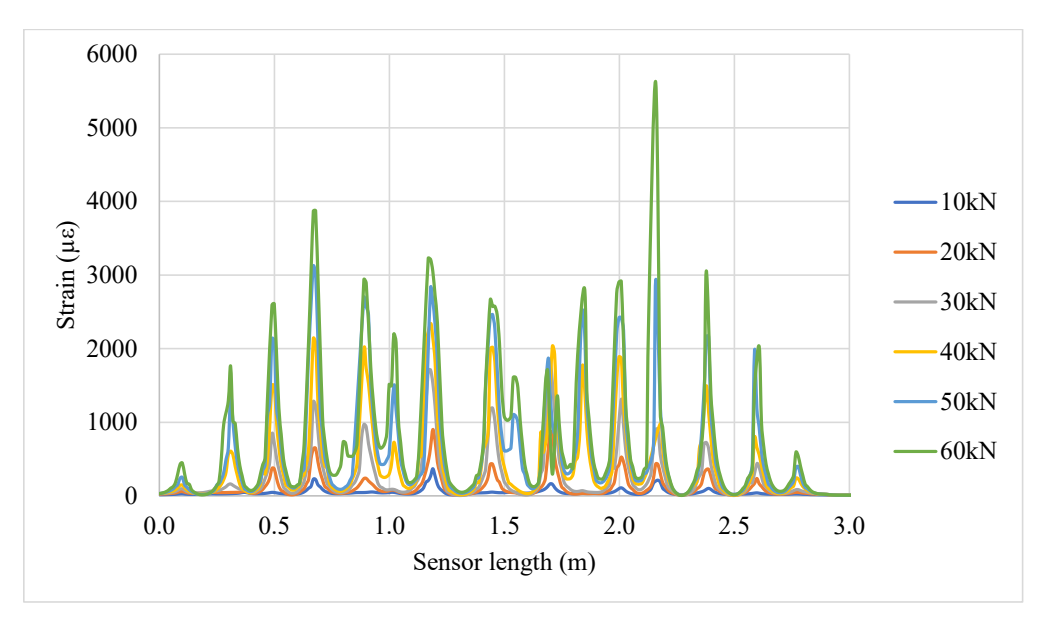


Figure A9. Surface strain along the side sensor length for beam R20C30.

References

- 1. Cai, X.; Chang, W.; Gao, L.; Zhou, C. Design and application of real-time monitoring system for service status of continuously welded turnout on the high-speed railway bridge. *J. Transp. Saf. Secur.* **2021**, *13*, 735–758. [CrossRef]
- 2. Weinstein, J.C.; Sanayei, M.; Brenner, B.R. Bridge damage identification using artificial neural networks. *J. Bridge Eng.* **2018**, 23, 04018084. [CrossRef]
- 3. Zhang, C.; Ge, Y.; Hu, Z.; Zhou, K.; Ren, G.; Wang, X. Research on deflection monitoring for long span cantilever bridge based on optical fiber sensing. *Opt. Fiber Technol.* **2019**, *53*, 102035. [CrossRef]
- 4. Ren, L.; Jiang, T.; Jia, Z.-g.; Li, D.-s.; Yuan, C.-l.; Li, H.-n. Pipeline corrosion and leakage monitoring based on the distributed optical fiber sensing technology. *Measurement* **2018**, *122*, 57–65. [CrossRef]
- 5. Xu, Y.; Li, J.; Zhang, M.; Yu, T.; Yan, B.; Zhou, X.; Yu, F.; Zhang, J.; Qiao, L.; Wang, T. Pipeline leak detection using Raman distributed fiber sensor with dynamic threshold identification method. *IEEE Sens. J.* **2020**, 20, 7870–7877. [CrossRef]
- 6. Vahdati, N.; Wang, X.; Shiryayev, O.; Rostron, P.; Yap, F.F. External corrosion detection of oil pipelines using fiber optics. *Sensors* **2020**, *20*, 684. [CrossRef]
- 7. Cao, B.-T.; Obel, M.; Freitag, S.; Mark, P.; Meschke, G. Artificial neural network surrogate modelling for real-time predictions and control of building damage during mechanised tunnelling. *Adv. Eng. Softw.* **2020**, *149*, 102869. [CrossRef]

Metrology **2025**, 5, 40 26 of 29

8. Moosazadeh, S.; Namazi, E.; Aghababaei, H.; Marto, A.; Mohamad, H.; Hajihassani, M. Prediction of building damage induced by tunnelling through an optimized artificial neural network. *Eng. Comput.* **2019**, *35*, 579–591. [CrossRef]

- 9. Gómez, J.; Casas, J.R.; Villalba, S. Structural Health Monitoring with Distributed Optical Fiber Sensors of tunnel lining affected by nearby construction activity. *Autom. Constr.* **2020**, *117*, 103261. [CrossRef]
- 10. Li, N.-L.; Jiang, S.-F.; Wu, M.-H.; Shen, S.; Zhang, Y. Deformation monitoring for Chinese traditional timber buildings using fiber Bragg grating sensors. *Sensors* **2018**, *18*, 1968. [CrossRef]
- 11. Oh, B.K.; Kim, K.J.; Kim, Y.; Park, H.S.; Adeli, H. Evolutionary learning based sustainable strain sensing model for structural health monitoring of high-rise buildings. *Appl. Soft Comput.* **2017**, *58*, 576–585. [CrossRef]
- 12. Fang, Z.; Su, H.; Ansari, F. Modal analysis of structures based on distributed measurement of dynamic strains with optical fibers. *Mech. Syst. Signal Process.* **2021**, *159*, 107835. [CrossRef]
- 13. Cao, W.; Wen, Z.; Su, H. Spatiotemporal clustering analysis and zonal prediction model for deformation behavior of super-high arch dams. *Expert Syst. Appl.* **2023**, *216*, 119439. [CrossRef]
- 14. Pathirage, C.S.N.; Li, J.; Li, L.; Hao, H.; Liu, W.; Ni, P. Structural damage identification based on autoencoder neural networks and deep learning. *Eng. Struct.* **2018**, 172, 13–28. [CrossRef]
- 15. Kurata, M.; Li, X.; Fujita, K.; Yamaguchi, M. Piezoelectric dynamic strain monitoring for detecting local seismic damage in steel buildings. *Smart Mater. Struct.* **2013**, 22, 115002. [CrossRef]
- 16. Suzuki, A.; Liao, W.; Shibata, D.; Yoshino, Y.; Kimura, Y.; Shimoi, N. Structural damage detection technique of secondary building components using piezoelectric sensors. *Buildings* **2023**, *13*, 2368. [CrossRef]
- 17. Yu, X.Y.; Li, X.; Li, Y.W. Estimating strain responses of beams in steel moment-resisting frames using limited acceleration data. *J. Civ. Struct. Health Monit.* 2025, 1–24. [CrossRef]
- 18. Ono, K. Review on structural health evaluation with acoustic emission. Appl. Sci. 2018, 8, 958. [CrossRef]
- 19. Yang, Y.; Zhang, Y.; Tan, X. Review on vibration-based structural health monitoring techniques and technical codes. *Symmetry* **2021**, *13*, 1998. [CrossRef]
- 20. Hasani, H.; Freddi, F. Operational modal analysis on bridges: A comprehensive review. Infrastructures. 2023, 8, 172. [CrossRef]
- Lu, P.; Phares, B. Integration of Structural Health Monitoring (SHM) into Multilayer Statewide Bridge Maintenance and Management Practices—SHM-Facilitated Condition-Based Maintenance (SHM-CBM) Prioritization System (No. 10-367); Midwest Transportation Center: Ames, IA, USA, 2018.
- 22. Lydon, M.; Taylor, S.; Lydon, D.; McFarland, B. The socio-economic benefits of Fiber optic strain based SHM of critical infrastructure. In Proceedings of the 9th European Workshop on Structural Health Monitoring, EWSHM 2018, Manchester, UK, 10–13 July 2018.
- 23. Bado, M.F.; Casas, J.R. A review of recent distributed optical fiber sensors applications for civil engineering structural health monitoring. *Sensors* **2021**, *21*, 1818. [CrossRef] [PubMed]
- 24. Mishra, M.; Lourenço, P.B.; Ramana, G.V. Structural health monitoring of civil engineering structures by using the internet of things: A review. *J. Build. Eng.* **2022**, *48*, 103954. [CrossRef]
- Seventekidis, P.; Giagopoulos, D.; Arailopoulos, A.; Markogiannaki, O. Structural Health Monitoring using deep learning with optimal finite element model generated data. Mech. Syst. Signal Process. 2020, 145, 106972. [CrossRef]
- 26. Kaushik, A.; Patnaik, G.; Rajput, A.; Prakash, G. Nonlinear behaviour of concrete under low-velocity impact by using a damaged plasticity model. *Iran. J. Sci. Technol. Trans. Civ. Eng.* **2022**, *46*, 3655–3677. [CrossRef]
- 27. Bi, J.; Huo, L.; Zhao, Y.; Qiao, H. Modified the smeared crack constitutive model of fiber reinforced concrete under uniaxial loading. *Constr. Build. Mater.* **2020**, 250, 118916. [CrossRef]
- 28. Minh, H.-L.; Khatir, S.; Wahab, M.A.; Cuong-Le, T. A concrete damage plasticity model for predicting the effects of compressive high-strength concrete under static and dynamic loads. *J. Build. Eng.* **2021**, *44*, 103239. [CrossRef]
- 29. Raza, A.; Ahmad, A. Numerical investigation of load-carrying capacity of GFRP-reinforced rectangular concrete members using CDP model in ABAQUS. *Adv. Civ. Eng.* **2019**, 1745341. [CrossRef]
- Seok, S.; Haikal, G.; Ramirez, J.A.; Lowes, L.N.; Lim, J. Finite element simulation of bond-zone behavior of pullout test of reinforcement embedded in concrete using concrete damage-plasticity model 2 (CDPM2). Eng. Struct. 2020, 221, 110984. [CrossRef]
- 31. Malekloo, A.; Ozer, E.; AlHamaydeh, M.; Girolami, M. Machine learning and structural health monitoring overview with emerging technology and high-dimensional data source highlights. *Struct. Health Monit.* **2022**, *21*, 1906–1955. [CrossRef]
- 32. Najafabadi, M.M.; Villanustre, F.; Khoshgoftaar, T.M.; Seliya, N.; Wald, R.; Muharemagic, E. Deep learning applications and challenges in big data analytics. *J. Big Data* **2015**, *2*, 1. [CrossRef]
- 33. Azimi, M.; Eslamlou, A.D.; Pekcan, G. Data-driven structural health monitoring and damage detection through deep learning: State-of-the-art review. *Sensors* **2020**, *20*, 2778. [CrossRef] [PubMed]

Metrology **2025**, 5, 40 27 of 29

- 34. Janiesch, C.; Zschech, P.; Heinrich, K. Machine learning and deep learning. Electron. Mark. 2021, 31, 685–695. [CrossRef]
- 35. Abdughani, M.; Ren, J.; Wu, L.; Yang, J.-M.; Zhao, J. Supervised deep learning in high energy phenomenology: A mini review. Commun. *Theor. Phys.* **2019**, *71*, 955. [CrossRef]
- 36. Yin, Y.; Antonio, J. Application of 3D laser scanning technology for image data processing in the protection of ancient building sites through deep learning. *Image Vis. Comput.* **2020**, *102*, 103969. [CrossRef]
- 37. Kim, H.; Ahn, E.; Shin, M.; Sim, S.-H. Crack and noncrack classification from concrete surface images using machine learning. *Struct. Health Monit.* **2019**, *18*, 725–738. [CrossRef]
- 38. Li, S.; Song, Y.; Zhou, G. Leak detection of water distribution pipeline subject to failure of socket joint based on acoustic emission and pattern recognition. *Measurement* **2018**, *115*, 39–44. [CrossRef]
- 39. Bai, X.; Wang, X.; Liu, X.; Liu, Q.; Song, J.; Sebe, N.; Kim, B. Explainable deep learning for efficient and robust pattern recognition: A survey of recent developments. *Pattern Recognit.* **2021**, *120*, 108102. [CrossRef]
- 40. Abdelaty, M.; Doriguzzi-Corin, R.; Siracusa, D. DAICS: A deep learning solution for anomaly detection in industrial control systems. *IEEE Trans. Emerg. Top. Comput.* **2021**, *10*, 1117–1129. [CrossRef]
- 41. Baccouche, A.; Ahmed, S.; Sierra-Sosa, D.; Elmaghraby, A. Malicious text identification: Deep learning from public comments and emails. *Information* **2020**, *11*, 312. [CrossRef]
- 42. Jayawickrema, U.; Herath, H.; Hettiarachchi, N.; Sooriyaarachchi, H.; Epaarachchi, J. Fibre-optic sensor and deep learning-based structural health monitoring systems for civil structures: A review. *Measurement* **2022**, 199, 111543. [CrossRef]
- 43. Siwowski, T.; Rajchel, M.; Howiacki, T.; Sieńko, R.; Bednarski, Ł. Distributed fibre optic sensors in FRP composite bridge monitoring: Validation through proof load tests. *Eng. Struct.* **2021**, 246, 113057. [CrossRef]
- 44. Kulpa, M.; Howiacki, T.; Wiater, A.; Siwowski, T.; Sieńko, R. Strain and displacement measurement based on distributed fibre optic sensing (DFOS) system integrated with FRP composite sandwich panel. *Measurement* **2021**, *175*, 109099. [CrossRef]
- 45. Berrocal, C.G.; Fernandez, I.; Bado, M.F.; Casas, J.R.; Rempling, R. Assessment and visualization of performance indicators of reinforced concrete beams by distributed optical fibre sensing. *Struct. Health Monit.* **2021**, *20*, 3309–3326. [CrossRef]
- 46. Tam, H.-y.; Lee, K.-k.; Liu, S.-y.; Cho, L.-h.; Cheng, K.-c. Intelligent optical fibre sensing networks facilitate shift to predictive maintenance in railway systems. In Proceedings of the 2018 International Conference on Intelligent Rail Transportation (ICIRT), Singapore, 12–14 December 2018; pp. 1–4.
- 47. Wang, Y.; Yao, H.; Wang, J.; Xin, X. Distributed optical fiber sensing system for large infrastructure temperature monitoring. *IEEE Internet Things J.* **2021**, *9*, 3333–3345. [CrossRef]
- 48. Khandel, O.; Soliman, M.; Floyd, R.W.; Murray, C.D. Performance assessment of prestressed concrete bridge girders using fiber optic sensors and artificial neural networks. *Struct. Infrastruct. Eng.* **2021**, *17*, 605–619. [CrossRef]
- 49. Bai, Y.; Xing, J.; Xie, F.; Liu, S.; Li, J. Detection and identification of external intrusion signals from 33 km optical fiber sensing system based on deep learning. *Opt. Fiber Technol.* **2019**, *53*, 102060. [CrossRef]
- 50. Li, S.; Peng, R.; Liu, Z. A surveillance system for urban buried pipeline subject to third-party threats based on fiber optic sensing and convolutional neural network. *Struct. Health Monit.* **2021**, *20*, 1704–1715. [CrossRef]
- 51. Jayawickrema, M.; Kumar, A.; Herath, M.; Hettiarachchi, N.; Sooriyaarachchi, H.; Epaarachchi, J. Strain patterns of short span reinforced concrete beams under flexural loading: A comparison between distributed sensing and concrete damaged plasticity modelling. *J. Intell. Mater. Syst. Struct.* **2023**, *34*, 1123–1135. [CrossRef]
- 52. Rodríguez, G.; Casas, J.R.; Villaba, S. Cracking assessment in concrete structures by distributed optical fiber. *Smart Mater. Struct.* **2015**, *24*, 035005. [CrossRef]
- 53. Yessoufou, F.; Zhu, J. Classification and regression-based convolutional neural network and long short-term memory configuration for bridge damage identification using long-term monitoring vibration data. *Struct. Health Monit.* **2023**, 22, 4027–4054. [CrossRef]
- 54. Torzoni, M.; Rosafalco, L.; Manzoni, A.; Mariani, S.; Corigliano, A. SHM under varying environmental conditions: An approach based on model order reduction and deep learning. *Comput. Struct.* **2022**, *266*, 106790. [CrossRef]
- 55. Jia, J.; Li, Y. Deep learning for structural health monitoring: Data, algorithms, applications, challenges, and trends. *Sensors* **2023**, 23, 8824. [CrossRef] [PubMed]
- 56. Cha, Y.J.; Ali, R.; Lewis, J.; Büyüköztürk, O. Deep learning-based structural health monitoring. *Autom. Constr.* **2024**, *161*, 105328. [CrossRef]
- 57. Rizvi, S.H.M.; Abbas, M. From data to insight, enhancing structural health monitoring using physics-informed machine learning and advanced data collection methods. *Eng. Res. Express.* **2023**, *5*, 032003. [CrossRef]
- 58. Schmidhuber, J. Deep learning in neural networks: An overview. Neural Netw. 2015, 61, 85–117. [CrossRef]
- 59. Bolourani, A.; Bitaraf, M.; Tak, A.N. Structural health monitoring of harbor caissons using support vector machine and principal component analysis. *Structures* **2021**, *33*, 4501–4513. [CrossRef]

Metrology **2025**, 5, 40 28 of 29

60. Kumar, K.; Biswas, P.K.; Dhang, N. Time series-based SHM using PCA with application to ASCE benchmark structure. *J. Civ. Struct. Health Monit.* **2020**, *10*, 899–911. [CrossRef]

- 61. Lv, M.Z.; Li, K.L.; Cai, J.Z.; Mao, J.; Gao, J.J.; Xu, H. Evaluation of landslide susceptibility based on SMOTE-Tomek sampling and machine learning algorithm. *PLoS ONE* **2025**, *20*, e0323487. [CrossRef]
- 62. Mbunge, E.; Sibiya, M.N.; Takavarasha, S.; Millham, R.C.; Chemhaka, G.; Muchemwa, B.; Dzinamarira, T. Implementation of ensemble machine learning classifiers to predict diarrhoea with SMOTEENN, SMOTE, and SMOTETomek class imbalance approaches. In Proceedings of the 2023 Conference on Information Communications Technology and Society (ICTAS), Durban, South Africa, 8–9 March 2023; IEEE: Piscataway, NJ, USA, 2023; pp. 1–6.
- 63. Neves, A.C.; Gonzalez, I.; Leander, J.; Karoumi, R. Structural health monitoring of bridges: A model-free ANN-based approach to damage detection. *J. Civ. Struct. Health Monit.* **2017**, *7*, 689–702. [CrossRef]
- 64. Yu, H.; Seno, A.H.; Sharif Khodaei, Z.; Aliabadi, M.F. Structural health monitoring impact classification method based on Bayesian neural network. *Polymers* **2022**, *14*, 3947. [CrossRef]
- 65. Tibaduiza Burgos, D.A.; Gomez Vargas, R.C.; Pedraza, C.; Agis, D.; Pozo, F. Damage identification in structural health monitoring: A brief review from its implementation to the use of data-driven applications. *Sensors* **2020**, *20*, 733. [CrossRef] [PubMed]
- 66. Saikia, P.; Baruah, R.D.; Singh, S.K.; Chaudhuri, P.K. Artificial Neural Networks in the domain of reservoir characterization: A review from shallow to deep models. *Comput. Geosci.* **2020**, *135*, 104357. [CrossRef]
- 67. Mangalathu, S.; Heo, G.; Jeon, J.-S. Artificial neural network based multi-dimensional fragility development of skewed concrete bridge classes. *Eng. Struct.* **2018**, *162*, 166–176. [CrossRef]
- 68. Xu, Y.; Bao, Y.; Chen, J.; Zuo, W.; Li, H. Surface fatigue crack identification in steel box girder of bridges by a deep fusion convolutional neural network based on consumer-grade camera images. *Struct. Health Monit.* **2019**, *18*, 653–674. [CrossRef]
- 69. Ma, R.; Zhang, Z.; Dong, Y.; Pan, Y. Deep learning based vehicle detection and classification methodology using strain sensors under bridge deck. *Sensors* **2020**, *20*, 5051. [CrossRef]
- 70. Rizzo, F.; Caracoglia, L. Artificial Neural Network model to predict the flutter velocity of suspension bridges. *Comput. Struct.* **2020**, 233, 106236. [CrossRef]
- 71. Wang, D.; Zhang, Y.; Pan, Y.; Peng, B.; Liu, H.; Ma, R. An automated inspection method for the steel box girder bottom of long-span bridges based on deep learning. *IEEE Access* **2020**, *8*, 94010–94023. [CrossRef]
- 72. Aktas, M.; Sumer, Y.; Agcakoca, E.; Yaman, Z. Nonlinear finite element modeling of composite bridge girders strengthened with HM-CFRP laminates. *Arab. J. Sci. Eng.* **2016**, *41*, 3783–3791. [CrossRef]
- 73. Theiner, Y.; Hofstetter, G. Numerical prediction of crack propagation and crack widths in concrete structures. *Eng. Struct.* **2009**, 31, 1832–1840. [CrossRef]
- 74. Sato, Y.; Naganuma, K. Discrete-like crack simulation by smeared crack-based FEM for reinforced concrete. *Earthq. Eng. Struct. Dyn.* **2007**, *36*, 2137–2152. [CrossRef]
- 75. Rimkus, A.; Cervenka, V.; Gribniak, V.; Cervenka, J. Uncertainty of the smeared crack model applied to RC beams. *Eng. Fract. Mech.* **2020**, 233, 107088. [CrossRef]
- 76. Genikomsou, A.S.; Polak, M.A. Damaged plasticity modelling of concrete in finite element analysis of reinforced concrete slabs. In Proceedings of the 9th International Conference on Fracture Mechanics of Concrete and Concrete Structures, Berkeley, CA, USA, 29 May–1 June 2016.
- 77. Tao, Y.; Chen, J.-F. Concrete damage plasticity model for modeling FRP-to-concrete bond behavior. *J. Compos. Constr.* **2015**, 19, 04014026. [CrossRef]
- 78. Hafezolghorani, M.; Hejazi, F.; Vaghei, R.; Jaafar, M.S.B.; Karimzade, K. Simplified damage plasticity model for concrete. *Struct. Eng. Int.* **2017**, 27, 68–78. [CrossRef]
- 79. Simulia. Abaqus 6.14 Analysis User's Guide. 2014. Available online: http://62.108.178.35:2080/v6.14/books/usb/default.htm (accessed on 29 June 2025).
- 80. Lee, S.-H.; Abolmaali, A.; Shin, K.-J.; Lee, H.-D. ABAQUS modeling for post-tensioned reinforced concrete beams. *J. Build. Eng.* **2020**, *30*, 101273. [CrossRef]
- 81. Béton, C.E.-I.d. CEB-FIP Model Code 1990: Design Code; Thomas Telford Publishing: London, UK, 1993.
- 82. Bhartiya, R.; Sahoo, D.R.; Verma, A. Modified damaged plasticity and variable confinement modelling of rectangular CFT columns. *J. Constr. Steel Res.* **2021**, *176*, 106426. [CrossRef]
- 83. Qingfu, L.; Wei, G.; Yihang, K. Parameter calculation and verification of concrete plastic damage model of ABAQUS. *IOP Conf. Ser. Mater. Sci. Eng.* **2020**, 794, 012036. [CrossRef]
- 84. Milligan, G.J.; Polak, M.A.; Zurell, C. Finite element analysis of punching shear behaviour of concrete slabs supported on rectangular columns. *Eng. Struct.* **2020**, 224, 111189. [CrossRef]
- 85. Reflectometer, Optical Backscatter. Optical Backscatter Reflectometer 4600 User Guide; Reflectometer, Optical Backscatter: Roanoke, VA, USA, 2013.

Metrology **2025**, 5, 40 29 of 29

86. Barrias, A.; Casas, J.R.; Villalba, S. Embedded distributed optical fiber sensors in reinforced concrete structures—A case study. Sensors 2018, 18, 980. [CrossRef]

87. Barrias, A.; Casas, J.R.; Villalba, S. Distributed optical fibre sensors in concrete structures: Performance of bonding adhesives and influence of spatial resolution. *Struct. Control Health Monit.* **2019**, 26, e2310. [CrossRef]

Disclaimer/Publisher's Note: The statements, opinions and data contained in all publications are solely those of the individual author(s) and contributor(s) and not of MDPI and/or the editor(s). MDPI and/or the editor(s) disclaim responsibility for any injury to people or property resulting from any ideas, methods, instructions or products referred to in the content.